CFD ANALYSIS OF THE INFLUENCE OF GUIDE VANES ON A ROOF MOUNTED VAWT WITH A DIFFUSER-SHAPED SHROUD AND FLANGE

HAMZA ABU-THURAIA

A Thesis

In the Department

of

Mechanical, Industrial and Aerospace Engineering

Presented in Partial Fulfilment of the Requirements

For the Degree of

Master of Applied Science (Mechanical Engineering)

Concordia University

Montréal, Quebec, Canada

May 2018

Concordia University

School of

Graduate Studies

This is to certify that the thesis prepared

By: **Hamza Abu-Thuraia**

Entitled: CFD Analysis of the Influence of Guide Vanes on a Roof Mounted VAWT With a Diffuser-Shaped Shroud and Flange

and submitted in partial fulfilment of the requirements for the degree of

Master of Applied Science (Mechanical Engineering)

complies with the regulation of the university and meets the acceptable standards with respect to originality and quality.

Signed by the final examining committee:

_____ (Chair)
Dr. Kudret Demirli

_____ (Examiner)
Dr. Charles Basenga Kiyanda

_____ (Examiner)
Dr. S. Samuel Li External
Building, Civil and Environmental Engineering

_____ (Supervisor)
Dr. Marius Paraschivoiu

Approved by _____
Dr. Mamoun Medraj, MASc Program Director
Department of Mechanical and Industrial Engineering

_____ / ____ / 2018

_____
Dr. Amir Asif, Dean Faculty of Engineering & Computer Science

Abstract

Advances in wind power and tidal power have grown considerably to offer a clean and sustainable energy alternative. Nevertheless, distributed small-scale energy production from wind in urban areas has been disappointing due to very low turbine efficiencies. Hence, it is the objective of this thesis to study and analyze the performance of a novel wind turbine design, a seven bladed Savonius vertical axis wind turbine (VAWT), which is horizontally oriented inside a diffuser-shaped shroud with a flange and attached with four deflectable guide vanes, mounted on the top of a building, which is shown to have the potential to achieve higher efficiencies. The flow field over the turbine is analyzed by using Computational Fluid Dynamics (CFD) Software Package of Star CCM+, on a three-dimensional (3D) grid for multiple tip speed ratio (TSR) at four different guide vane angles of 35°, 45°, 55° and 65°, while keeping all vanes open. Another case was analyzed where selected vanes would be open while closing others. In this work, the wind flow directly facing the turbine is studied to compute the coefficient of power C_p. The coefficient of power with detachable guide vane attached was found to be 0.333 at vane angle of 55°. Finally, the most effective case is when the bottom vane is closed compared to the bottom two vanes closed. This case with only one closed vane achieves a maximum C_p value of 0.398.

AKNOWLEDGMENT

Alhamdulillah, all praises to Allah for the strength and guidance. I would like to express my sincere appreciation to my supervisor, Dr. Marius Paraschivoiu, who has given me this opportunity and for his constant support and encouragement. His timely advice, scrutiny and patient approach have motivated me in overcoming many obstacles along the way. It was definitely a privilege working with him.

I would like to thank Dr. Cevdet Aygun and my colleagues in the lab for their helpful suggestions along the way. I also extend my gratitude to the ENCS department at Concordia University, for providing me with the necessary facilities to complete my research.

I am also sincerely grateful to my MechBros Tutoring colleagues and students for the constant support and encouragement. A special mention to my dear friends Amit Bains, Yahya Abdullahi and Emad Haneef.

Finally, I am forever grateful to have the support of my parents, Nabil Abu-Thuraia & Shamieh Al-Khateeb and my siblings for the unconditional love and support. They are the reason I am here. I dedicate this thesis to my parents and my siblings.

CONTENTS

LIST OF FIGURES

LIST OF TABLES

NOMENCLATURE

SYMBOL	PROPERTY
$\vec{u}$	Velocity vector
P	Pressure
$\vec{F}$	Force Vector
ρ	Density of air
μ	Dynamic viscosity of air
$\bar{P}$	Mean pressure
p'	Fluctuating components of pressure term
U_i	Mean velocity
$u_i{}'$	Fluctuating component of velocity
S_{ij}	Reynolds's stress tensor
μ_τ	Eddy viscosity
k	Turbulent kinetic energy
ε	Turbulent dissipation rate
G_k	Turbulent kinetic energy production from mean flow velocity gradient
G_b	Turbulent kinetic energy production from buoyancy
Y_M	Fluctuating dilation in compressible turbulence to dissipation rate
S_k, S_ε	Source terms
$C_1, C_{1\varepsilon}$	Constants
σ_ε	Prandtl number
λ	Tip speed ratio

C_D	Coefficient of drag
V_∞	Free stream velocity
ω	Angular speed of turbine rotor
R	Blade tip radius of rotor
C_p	Coefficient of power
A	Swept area of turbine
H'	Height of building
C_m	Coefficient of moment
Ω	Rotational angle
$\emptyset$	Guide vane angle

CHAPTER 1: INTRODUCTION

1.1 Importance of Renewable Energy

Energy is one of the most important resources for humans, because it is essential in all sectors of our economy, such as in industry, transportation, agriculture, communication and so on. Currently, energy consumption is heavily based on the burning of fossil fuels such as coal, oil, and natural gas, which are all non-renewable resources [1]. The latter is a problem because the use and dependency on these resources have many major health and environmental consequences. In particular, the burning of fossil fuels releases toxins and has been linked to high carbon dioxide emissions that pollute the atmosphere and contribute to global warming. It is also linked to extensive land degradation, as well as asthma and cancer. As such, costs accrue at every point along the fossil fuel supply chain. Extraction of fossil fuels can cause air and water pollution, and harm local communities [1]. Transporting fuels can cause air pollution and lead to accidental spills. Once the fuels are burned, they emit toxins and the waste products are hazardous to public health and the environment. Additional issues surrounding reliance of fossil fuels include price fluctuations and concerns regarding security of supply.

Energy consumption and waste emissions are an issue of concern today, and sustainable development is in the forefront of public awareness. Since the dependency of fossil fuels is not practical in the long term, nonconventional energy resources have been proposed as a solution. Renewable energy resources, such as solar power, wind power, hydropower, biomass, and geothermal, have been explored as potential solutions for a sustainable energy future [2]. There are many advantages to using renewable energy, such as minimizing safety issues [3] and climate change by reducing greenhouse gas emissions. There are also no process costs and equipment required to collect renewable energy resources since they are sustainable, free, and practically omnipresent.

With the demand of electricity increasing twice as fast as overall energy use, and since it is likely to rise 76 percent by 2030 (from 2010) [4], society is becoming increasingly aware of the need for renewable energy over the last few years; more countries are starting to shift their energy resources

to renewable energy sources [5]. According to the NREL Renewable Electricity Futures Study, renewable energy will be adequate to fulfil 80 percent of U.S's electricity needs by 2050 [6].

Although renewable energy has many advantages, it is also important to consider its disadvantages. First, choosing the right type of renewable energy for a particular region is necessary. Most important factors to consider include costs associated with electricity generation, efficiency of the energy system chosen, land and water requirements, as well as social and economic impact regarding its implementation [7]. In the following section, we will explore one specific renewable form of energy, wind energy, in great detail, since this form is most relevant to the thesis project.

1.2 Importance of Wind Energy

After hydropower, wind energy is the second major source of renewable energy [8]. In 2008, 1.5% of worldwide electricity was provided by wind turbines. Over the next two decades, there will be a lot of promise for growth in the wind energy industry [9]. It has been concluded that wind power provides approximately one-sixth of the world's electricity, accounting for land and off-shore wind farms, as well as industrial wind turbines.

Although there are disadvantages to the utilization of wind energy, these disadvantages are outweighed by the multitude of disadvantages associated with other forms of renewable energy; in particular, those associated with solar energy, hydropower, nuclear power, and geothermal [10].

The initial costs associated with solar energy are incredibly high, due to purchasing and installation of solar panels. Solar panels require large installation areas and must be installed in areas with clear skies, not to mention that they are also useless during the nighttime. Moreover, the photovoltaic panels are made toxic metals, such as mercury, lead, and cadmium, which would have detrimental effects on the environment. Their efficiency is susceptible to pollution.

Just like installation in solar energy and hydropower are expensive, so too is the installation of nuclear power stations. Nuclear power stations take between five to ten years to construct. Waste produced by nuclear reactors is hazardous and can leak radiation. There is a significant risk of a nuclear accident, such as Chernobyl, for instance. Also, the reactors have a significant impact on

human and marine life. Furthermore, uranium is a scarce resource and only a few countries have it, so it is not the most reliable of renewable sources.

Geothermal energy also has high installation costs, not to mention the fact that it is not a widespread energy source. If there is a drop-in temperature or if too much water is injected to cool the rocks, the consequence is that the geothermal sites can run out of steam over a certain timespan. Geothermal energy is only adequate for regions that have very hot rocks below Earth, and the sites may contain poisonous gases. In addition, transportation of geothermal energy is challenging, and once the energy is extracted, use of it is limited to surrounding areas only.

1.3 Types of Wind Turbines

Wind turbines are classified according to their axis of rotation. The two main types of wind turbines are the following: Horizontal Axis Wind Turbines (HAWTs) and Vertical Axis Wind Turbines (VAWTs). At present, most turbines that have been installed are classified as HAWTs. Nevertheless, there are many advantages of VAWTs which make them useful for urban areas. A VAWT is a wind turbine whose main rotor is located vertically, and the gear box is placed on ground. Thus, when comparing with HAWTs, maintenance and repair level compliance are easier. VAWTs can also be placed in close proximity to each other, whereas in HAWTs more space is used. As well, less noise is produced in VAWTs, and the initial speed required to move the blades is lower. In contrast, HAWTs yield better performance in uniform wind, but lessens as wind direction fluctuates [11]. As such, VAWTs accommodate any kind of wind direction, non-uniformity, and/or rapid wind fluctuations, and dirty winds don't greatly influence their performance [12]. As well, the fabrication of VAWTs is easier than HAWTs, because VAWT blades have a uniform and untwisted profile; in contrast, HAWTs have blades that are tapered and twisted for optimal efficiency. Major disadvantages include a lack of self-starting capability, high torque fluctuations within each revolution cycle, and dynamic stall and fatigue failure may occur due to the wind turbine's rotational motion [13].

Horizontal Axis Wind Turbine		Vertical Axis Wind Turbine	
Advantages	*Disadvantages*	*Advantages*	*Disadvantages*
Provide better performance in uniform wind	Noise	Performs better as wind direction fluctuates	Low wind speeds due to self-starting
High Efficiency	High construction and installation cost	Less Noise	High turbulence intensity
Variable blade pitch, giving different angles of attack	Large size can disturb landscapes of certain cities	Easier Maintenance	Needs to be placed on high altitudes to not reduce the power coefficient

Table 1: Summary of advantages and disadvantages of urban based wind turbines [14]

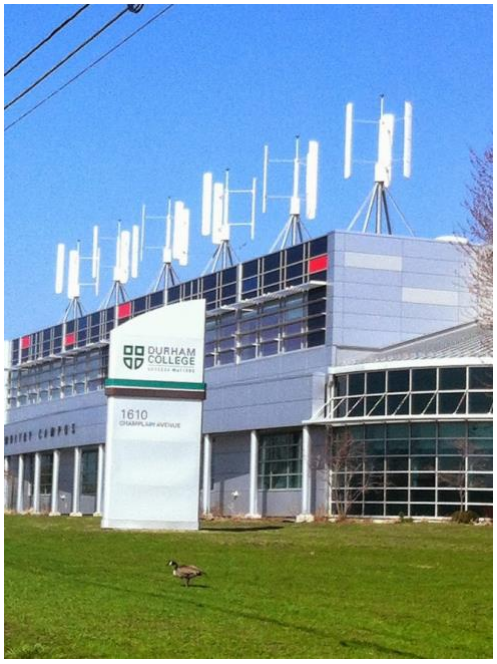

Fig 1. (A)


Fig 2. (B)

Figure 1: (a) Rooftop mounted VAWTs in Durham College, Whitby (b) Three HAWTs attached to the World Trade Center in Bahrain [48]

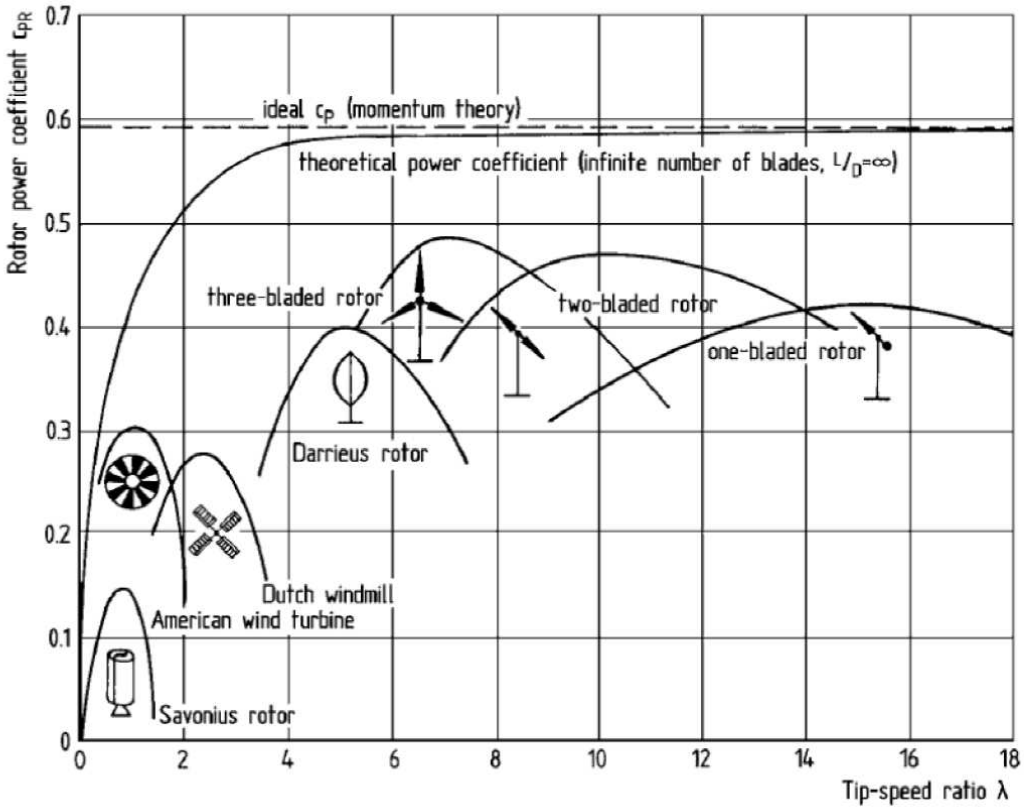

Figure 2: Power Coefficients for Different Rotor Designs [15]

Savonius turbines are drag based vertical axis wind turbines that consist of two semi cylindrical blades put together in the form of an S-shape. In comparison to other VAWTs, the Savonius turbine has a low cut-in speed to begin to rotate and generate power, though it presents the lowest coefficient of power [42] as shown in Figure 2. Nonetheless, its application is appealing due to its simplicity, low cost, safer speeds, and its suitability for roof mounting.

Some of the major parameters used in the analysis of wind turbines are the tip speed ratio (TSR), and the coefficients of the moment (ie. torque), and the power. The TSR of the turbine is the ratio of the tip speed of the blade to the free stream velocity which is defined as

$$TSR = \frac{R*\omega}{V_\infty}, \tag{1.1}$$

where V_∞ is the free stream velocity at the height of the turbine, R is the turbine radius and $\boldsymbol{\omega}$ is the angular velocity of the turbine which is held constant for each simulation. Power is given as

$$Power = (M * \omega), \tag{1.2}$$

where M represents the average torque per rotation at the rotor shaft. Coefficients of the moment and power are defined as

$$Cm = \frac{M}{0.5*\rho*V_\infty^2*A*R}, \tag{1.3}$$

and

$$Cp = \frac{(M*\omega)}{0.5*\rho*V_\infty^3*A} = Cm * TSR, \tag{1.4}$$

where $\boldsymbol{\rho}$ is the air density, A is the swept area of the turbine equal to $H * 2R$ *(depth)*, and H is the height of the turbine.

1.4 Safety

The design lifetime of a standard HAWT is about 20 years, over which they have to be operating safely and reliably in hazardous weather conditions. Wind turbines are built to withstand wind speeds around 150 miles per hour. Anything around 200-250 mph, the turbines will require some type of safety to stop and prevent overheating and exploding. Since 1972, 75 turbines have been reported to be damaged in the US according to the department of labor due to severe wind conditions [16].

For safety purposes, most HAWT use multiple ways to stop the blades from rotating during harsh wind conditions by either pitching the blades, yawing or applying emergency brakes to the rotor. For VAWTs, blades cannot really pitch like HAWT's but some of them do use other mechanisms such as rotor locks to stop any movement. For simplicity and cost purposes for this project, other design options are needed [17].

1.5 Design work related to VAWT

Use of the wind turbines is long known to be a practical method to capture and convert the energy of the wind into mechanical and electrical energy [18]. In this sense, small-scale wind turbines

have a great potential to become widespread in urban areas for the wind-based electricity generation, as pointed out by Acoste et al. [19]. Bahaj et al. [20] stated that such turbines may soon become a commercial reality as a result of both advancements in technology and new financial incentives. Computational Fluid Dynamics (CFD) tools are utilized worldwide in an effective manner for the flow analysis and the design of the wind turbines including vertical ones. Since the accuracy of the numerical simulation depends on the spatial discretization and the order of the discretization method, Naghip et al. [21] carried out a mesh convergence study for simulating the flow around vertical axis wind turbines and showed that CFD can be used efficiently to calculate their coefficient of power.

The research in the field of small-scale wind turbine improvements recently examined ways to increase their performances and to make them more efficient on building roofs. Ledo et al. [22] found that turbines mounted on flat roofs are likely to yield higher and more consistent power for the same turbine hub elevation than for other roof profiles. For small-scale vertical axis wind turbines mounted on the roofs of buildings, one of the design challenges is related to a lack of exposure to strong enough winds which results in low power generation. However, Dragorimescu et al. [23] demonstrated that it is possible to increase the power coefficient C_p of small-scale turbines by developing new designs so that they generate more electrical power under low wind conditions.

Much research was conducted on wind or air flow surrounding buildings. For instance, Holdredge et al. [27] and Evans et al. [28] studied air flow above buildings and determined a positive pressure zone was created on the upstream side, while a negative pressure zone (recirculation zones) were created on the roof and on all the other sides of the building. For air flow perpendicular to the windward wall, the height of the roof recirculation zone may be between 1.3-2 times the building height of conventional, one and two-storey, industrial buildings. In many buildings, the cavity will extend over the full roof of the building. If the building is very long in the wind direction, the air flow will reattach to the roof. Moreover, Song et al. [29] evaluated the large-scale vortex structure and the characteristics of unsteady flow around a tall building. Their research found that a horse-shoe vortex develops in the vicinity of the building. Twin axial vortices are produced by the roof

side edges, which are strengthened by the downwash from the main stream. Furthermore, there is unsteady vortex shedding on the vertical plane of symmetry, induced by Karman vortex shedding.

To simulate urban wind environment, Azli Abd Razak et al. [30] did a Large Eddy Simulation (LES) using five different types of uniform staggered building arrays. They realized that the frontal area ratio is the most important parameter that influences pedestrian wind environment. The frontal area ratio is measured as the product of the plan area ratio and building aspect ratio. To forecast pedestrian wind environment, an exponential equation was derived using the frontal area ratio. Abohela et al. [31] indicated that an increase of up to 56.1% in energy output can be achieved on roof mounted wind turbines, with a vaulted roof, and an informed wind assessment. Nevertheless, the turbine used was not shrouded. Abohela et al. [31] showed that the roof shape, wind direction, building height, and urban configuration have an effect on the energy yield and the technology of positioning of roof mounted wind turbines, which presents a high potential for integration within the built environment. Thus, it is important to inform developers of which roof shape to use and to orient the building such that the roof mounted wind turbine would benefit from the prevailing wind direction and its interaction with the proposed roof shape. The novelty of this study is that every simulation conducted is the turbine with guide vanes and a building. Therefore, all of the effects of the building can be considered and can also benefit the turbine design.

Ohya et al. [32] and Dilimulati et al. [33] showed that to enclose the turbine in a diffuser-shaped shroud and to integrate the shroud with a broad brim (flange) at the exit constitutes an efficient solution to raise the total power coefficient C_p of the turbine. The C_p is raised by creating a low–pressure region due to a strong vortex formation behind the brim and by doing so, drawing more mass flow into the diffuser shroud. Matsushima et al. [34] experimentally and numerically proposed a frustum-shaped diffuser for small wind turbines that presented a maximum wind speed increase of 1.7 times and an output power of 2.4 times more than the conventional turbine. The diffuser preformed at its best when the wind direction was constant. Moreover, El-Zahaby et al. [35] studied different flange angles for a diffuser-shaped, shrouded, small-scale wind turbine. It was shown that there was a 5% increase in generated power compared to a normal flange.

1.5.1 Previous Design

Larin et al. [36] studied a horizontally oriented, bare Savonius (without shroud) wind turbines with two blades and seven blades, mounted on the upstream edge of a flat building roof. They used ANSYS Fluent software package as the CFD tool to analyze the flow around the turbine, computational domain of which was simulated by using a grid of five million elements with 500 time steps per rotation (0.72° per time step) and by applying the symmetry condition at the mid-plane, to halve the domain. They were able to show that the power coefficient of the building mounted seven bladed turbine with double 30° cut blades at a tip speed ratio of 0.5, improved to 0.24 from 0.043 which is the power coefficient of a seven-bladed turbine without cuts placed in a freestream, representing an improvement of 450%.

Complementing this work, Krishnan et al. [37] studied the seven bladed horizontally oriented VAWTs enclosed in diffuser-shaped shrouds with the flanges at the exit, mounted on the upstream edge of a flat building roof. They performed a non-dimensional parametric study on each of the design parameters of the components, taking the coefficient of power C_p as key variable, and optimized its design. They also used ANSYS Fluent software package as CFD tool to analyze the flow around the turbine. The computational domain was simulated by using a grid of 6.8 million elements with a time step of 0.02 seconds and the symmetry condition was applied at the mid-plane, to halve the domain. As a result of this analysis, they found out that power coefficient C_p improved from 0.135 of the original prototype, to 0.34 of the final design with a cut of 30° to the end of the blades, at a tip speed ratio of 0.38.

1.5.2 CFD Considerations

In several wind turbine simulations, CFD analysis was used to predict performance. To achieve a high level of accuracy, CFD must be set up correctly. After reviewing the latest numerical calculations of wind turbine wake aerodynamics, Sanderse et al. [24] discussed CFD techniques for modeling the turbine's rotor and wake. Mainly, they focused on the wake effect on downstream turbines. Song et al. [25] studied, in 2D, four meshing strategies and six different turbulence model selections for VAWT simulations. Their research determined that the realizable $k-\epsilon$ model is the closest CFD simulation of the experimental model and predicts the best performance. Their

research also indicated that the rotation angle in each time step should not exceed two degrees. Then, Sagol et al. [26] studied prediction using two-equation turbulence models in ANSYS FLUENT for an NREL Phase VI HAWT rotor, for a specific wind speed. Sagol et al. concluded that the $k-\omega$ SST model was most appropriate. This model is considered as the industrial standard, but it has strict mesh requirements, and has a higher computational cost and time.

Furthermore, Larin et al. [36] and Belkacem et al. [50] studied multiple turbulence models and techniques for a conventional drag based savonius rotor to validate their CFD simulations with experimental results from Hayashi [40]. Larin et al. discuss in 2D, three different meshing techniques and four different turbulent models in comparison to the experimental results at multiple TSR values. It was determined from the research that the coarse mesh with enhanced wall function and realizable $k-\epsilon$ as the turbulence model performed the closest results to the experimental. It was also concluded by Belkacem, that realizable $k-\epsilon$ with constant wind speed of 6m/s, 9m/s and 12m/s deemed to be acceptable at higher TSR values with the experimental results.

Samson et al. [51] studied a lift based Darrieus wind turbine on a roof of a building by validating the CFD results with experimental results conducted by Sheldahl et al. [52]. By selecting k – ω SST turbulence model and a selective meshing methodology, Samson achieved similar results to the experimental results as that validated the CFD analysis.

1.5.3 Deflectors/Obstacle

As Savonius rotors are proven to have insufficient coefficient of power, obstacles or external geometries are sometimes used to increase the Cp. Typically, the objective is to decrease the drag of the returning blade by considering the external geometry, while increasing the drag on the advancing blade, and consequently, increasing the net torque of the turbine. Such techniques suggest that increasing the coefficient of power closer to that of other VAWT is possible, making the Savonius turbines more attractive for commercial use. In addition to increasing power, external geometries also ameliorate self-starting capability of the turbine by increasing static torque.
As shown in Figure 3, Mohamed et al. [38] showed that flat obstacle shielding can impact turbine performance [38]. For two to three blade turbines, the optimal configuration led to a coefficient of

power increase of 27.3% and 27.5%, respectively. Mohamed also presented a relative increase in coefficient of power of 47.8% using a deflector with an obstacle at optimal TSR, and improvement of approximately 30% in the turbine's operating range.

Furthermore, Wahyudi et al. [39] proposed a two-bladed turbine with moving deflectors to increase the velocity and the efficiency of the turbine. It was concluded that the deflectors lead to positive torque. Hayashi et al. [40] proposed a three stage Savonius rotor with guide vanes. It was shown that the addition of guide vanes increased the static torque, whereas the coefficient of torque increased only in the lower range of TSR values and decreased in higher range of TSR values.

Belkacem et al. [50] studied, in three-dimensions, a selection of different farms of conventional Savonius wind turbines placed in a linear array. With the performance of these farms proven to be ineffective, an obstacle was added to deflect the wind towards the array of turbines. As a result of this addition, there was an improvement of 10% to the power coefficient.

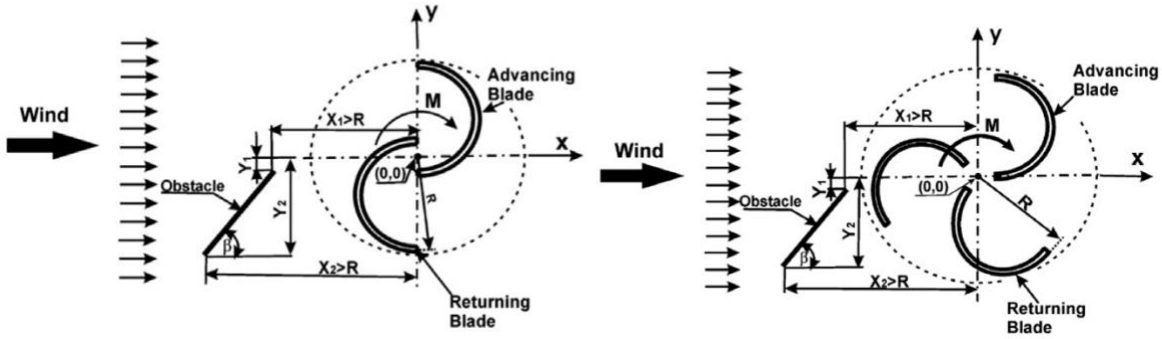

Figure 3: Obstacles used on two(left) and three(right) blade savonius [38].

Patankar et al. [41] proposed a CFD investigation of a hybrid solar and wind system that is simulated on rooftops of different heights and locations of buildings. The system doesn't only take advantage of the accelerated flow over a building but utilizes its vertical and horizontal louvers to capture low winds and accelerate it through the vertical axis turbine, as shown in Figure 4. It was further concluded that Cp increased by a factor of 1.7.

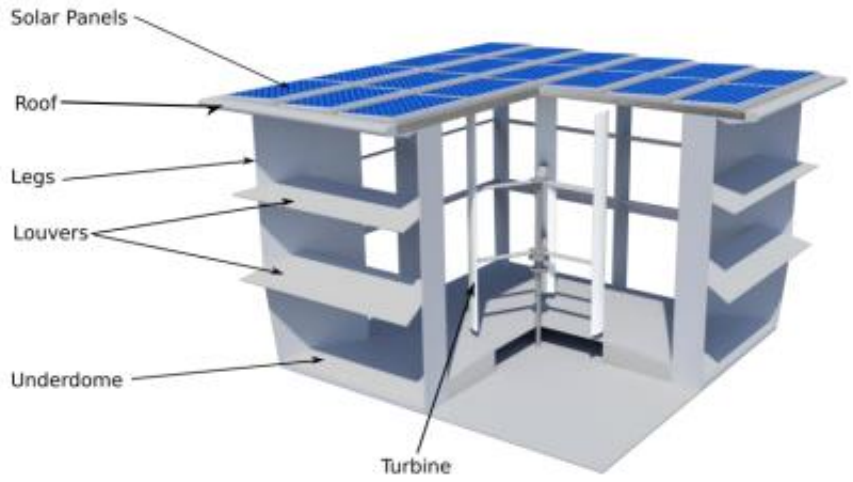

Figure 4: PowerNEST concept [41]

1.6 Aerodynamic Brakes

As there are different methods to address overspeed protection in wind turbines, such as stall, and yaw controls, variable pitch and aerodynamic brakes can be the most relevant to the Savonius turbine with detachable guide vanes. In horizontal axis wind turbines, certain extra parts are required for them to work based on the centrifugal force. These parts are placed at the edge or in the middle of the blade and cause resistance to the blade motion, thus slowing it down [42]. Furthermore, another concept slowing down wind speeds is variable pitch control. Variable pitch controls rotate the turbine blades around the blade center line to control the generator rotational speed. This concept will be applied in the proposed design of the roof mounted VAWT with guide vanes as presented in chapter 3.

1.7 Motivation

With the surge of utilizing renewable energy, it is vital to seek advancements in aspects of engineering design. With wind power generation being proportional to the wind speed cubed, in stormy condition the turbine must be stopped. By designing a mechanism to allow power generation in all conditions, using mechanical devices, the power of a wind turbine can be maintained at all times. This advancement allows for power to be used in a more efficient way.

One such method is the deflector/obstacle concept, which is discussed later in the thesis. It is also applied to the turbine being studied and is seen to aid in the generation of power, inhibiting much power loss.

Hence, the motivation behind this research is to propose a viable way to generate electricity at all times, with the application of a safety mechanism, and utilize the advantages of location associated with the roof of the building, to minimize power loss.

1.8 Objective

In this thesis, as a continuation of the building mounted seven-bladed diffuser-shaped shroud VAWT from Krishnan [37] and Larin [36], it is proposed to study the effects of attaching guide vanes at the entrance of the diffuser-shaped shroud, which encloses the rotating turbine inside. It is anticipated that attaching deflectable guide vanes at the entrance of the shroud and flange system which encloses the rotating turbine, will provide certain advantages. The first of these advantages is that it provides a mean to close the turbine which serves as a safety precaution in stormy weather. The second advantage of the guide vanes is that the flow can be reduced at high wind so that the turbine can continue to operate. Thus, it is the purpose of this thesis to study and analyze the performance of a novel wind turbine design consisting of a seven-bladed wind turbine enclosed inside a diffuser-shaped shroud, with the four deflectable guide vanes attached at the entrance of the shroud and with a flange attached at the exit. The use of the deflectable guide vanes allows to simulate the flow of the wind around the system not only for the case of inflow through the vanes at preselected vane angles of 35°, 45°, 55°, and 65°, but also for the case of inflow through the vanes when keeping some of the vanes closed and keeping the remaining ones open at any vane angle. Also, instead of closing the vanes completely during high winds that may cause damage to the turbine, they can be opened at a low angle to still allow for power generation. Additionally, this thesis will report the effects of keeping certain vanes open while closing others. A 3D view of the proposed assembly of the diffuser-shaped shroud enclosing the wind turbine hidden in it, with the guide vanes attached in the front and the flange at the exit, is illustrated in Figure 5. Freestream wind blows from left to right along the x-axis with an inflow component through the guide vanes into the shroud.

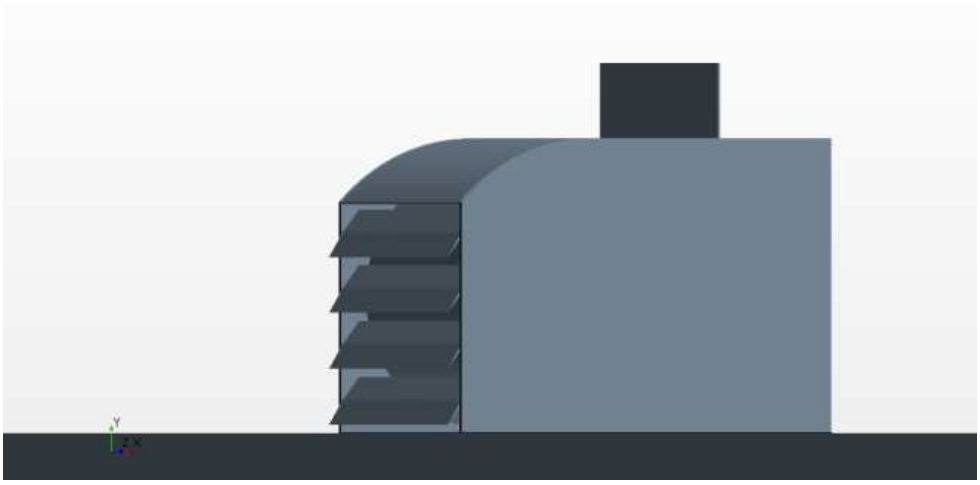

Figure 5: Exterior of the diffuser-shaped shroud which accommodates the rotating turbine inside, with four guide vanes attached at the entrance and the flange (brim) at the exit. Direction of the wind is from left to right along the x-axis.

Chapter 2: Methodology Validation

2.1 Governing Equations

To solve the flow, the Navier-Stokes equations must be numerically solved. Having the assumption that flow over the roof top mounted VAWT is incompressible and transient, we must start with the continuity and momentum equation [43]:

$$\nabla \cdot \vec{u} = 0 \tag{2.1}$$

$$\frac{\partial \vec{u}}{\partial t} + (\vec{u} \cdot \nabla)\vec{u} = -\frac{1}{\rho}\nabla P + \frac{\mu}{\rho}\nabla^2 \vec{u} + \vec{F} \tag{2.2}$$

Equation 2.1 and 2.2 can be rewritten as:

$$\frac{\partial u_i}{\partial x_i} = 0 \tag{2.3}$$

$$\rho \frac{\partial u_i}{\partial t} + \rho \frac{\partial}{\partial x_j}(u_i u_j) = -\frac{\partial p}{\partial x_j} + \mu \frac{\partial^2 u_i}{\partial x_j} \tag{2.4}$$

where $i, j = 1,2, or\ 3$

As turbulence consists of various flow properties that have random fluctuations, it must be treated using a statistical approach. Unsteady Reynolds-Averaged Navier Stokes (URANS), Large Eddy Simulation (LES) or Direct Numerical Simulation (DNS) are the popular options to model the turbulence. LES is more advanced than URANS but requires much better mesh and has a very high computational cost, which isn't reasonable with our simulation. Direct Numerical Simulation requires a very small time step and very fine grid requirements. For our requirements and previous research on the turbine, URANS best fit our needs and is less computationally expensive.

With the URANS equations being the time averaged equations of motion of fluid flow, Reynolds decomposition is needed to decompose equations 2.3 and 2.4 into their mean values and fluctuations with zero mean as shown in equation 2.5 and 2.6 [43].

$$u_i = U_i + u_i' \tag{2.5}$$

$$p = \bar{P} + p' \tag{2.6}$$

The Reynolds averaged equations in conservation form are given by:

$$\frac{\partial U_i}{\partial x_i} = 0 \tag{2.7}$$

$$\rho \frac{\partial U_i}{\partial t} + \rho \frac{\partial}{\partial x_j}\left(U_j U_i + \overline{u_\iota{}' u_J{}'}\right) = -\frac{\partial P}{\partial x_j} + \frac{\partial}{\partial x_j}\left(2\mu S_{ij}\right) \tag{2.8}$$

Where U_i is the mean velocity in the i direction, u_i' is the velocity fluctuation in the i direction, $-\overline{u_\iota{}' u_J{}'} = \tau_{ij}$ is the specific Reynolds Stress tensor and S_{ij} is the mean strain rate tensor which is expressed as:

$$S_{ij} = \frac{1}{2}\left(\frac{\partial u_i}{\partial x_j} + \frac{\partial u_j}{\partial x_i}\right) \tag{2.9}$$

From Boussinesq approximation, the eddy viscosity by the relation:

$$-\rho\overline{u_\iota{}' u_J{}'} = \rho\mu_t\left(\frac{\partial U}{dy} + \frac{\partial V}{dx}\right) \tag{2.10}$$

After Simplifying equation 2.8, we achieve the URANS expression in common form.

$$\rho \frac{\partial U_i}{\partial t} + \rho U_j \frac{\partial U_i}{\partial x_j} = -\frac{\partial P}{\partial x_j} + \frac{\partial}{\partial x_j}\left(2\mu S_{ij} - \rho\overline{u_\iota{}' u_J{}'}\right) \tag{2.11}$$

For general three-dimensional flows, there are a total of ten unknown components in the URANS equations. In addition to six unknown Reynolds Stress components, four mean-flow components, three in the velocity components (U, V, W) and pressure. Turbulence modeling will allow us to calculate turbulent eddy viscosity and model the Reynolds stress tensor in terms of the mean flow quantities, thus providing us with closure to the governing equations.

2.1.1 Realizable K-ε Model

From URANS based turbulence models, a 3D simulation with flow separation and multiple rotational flows is sufficiently more efficient and affordable than the LES and DNS models. From the two-equation models, the realizable k-ε was chosen for multiple applications, as its recirculation, strong pressure gradients and flow separation serve well for drag based turbines.
The transport equation for the turbulence kinetic energy k and the turbulence dissipation rate ε in realizable k-ε model [43]:

$$\frac{\partial(\rho k)}{\partial t} + \frac{\partial(\rho k u_j)}{\partial x_j} = \frac{\partial}{\partial x_j}\left[\left(\mu + \frac{\mu_t}{\sigma_k}\right)\frac{\partial k}{\partial x_j}\right] + G_k + G_b + \rho\varepsilon - Y_M + S_k \tag{2.12}$$

and

$$\frac{\partial(\rho\varepsilon)}{\partial t}+\frac{\partial(\rho\varepsilon u_j)}{\partial x_j}=\frac{\partial}{\partial x_j}\left[\left(\mu+\frac{\mu_t}{\sigma_\varepsilon}\right)\frac{\partial\varepsilon}{\partial x_j}\right]+\rho C_1 S_\varepsilon-\rho C_2\frac{\varepsilon^2}{k+\sqrt{\nu\varepsilon}}+\frac{C_{1\varepsilon}\varepsilon}{k}C_{3\varepsilon}G_b+S_\varepsilon \tag{2.13}$$

where

$$C_1=\max\left[0.43,\frac{\eta}{\eta+5}\right] \tag{2.14}$$

$$\eta=\frac{Sk}{\varepsilon} \tag{2.15}$$

$$S=\sqrt{2S_{ij}S_{ij}} \tag{2.16}$$

$$\mu_t=\rho C_\mu\frac{k^2}{\varepsilon} \tag{2.17}$$

In the realizable k-epsilon, the critical coefficient of the model C_μ is expressed as a function of mean flow and turbulent properties rather than a constant as in the standard k-epsilon model

$$C_\mu=\frac{1}{A_0+A_S\frac{kU^*}{\varepsilon}}\ , \tag{2.18}$$

where

$$U^*=\sqrt{S_{ij}S_{ij}-\widetilde{\Omega_{ij}}\widetilde{\Omega_{ij}}}\ , \tag{2.19}$$

and

$$\widetilde{\Omega_{ij}}=\Omega_{ij}-2\varepsilon_{ijk}\omega_k\ , \tag{2.20}$$

$$\Omega_{ij}=\overline{\Omega_{ij}}-\varepsilon_{ijk}\omega_k\ . \tag{2.21}$$

2.2 Wall Treatment

The walls are a source of vorticity in our practical simulation, and thus, it is important to accurately predict the flow and turbulence properties across the wall boundary layer. The non-dimensional wall distance y^+ is given as

$$y^+=\frac{yu^*}{\nu}\ , \tag{2.22}$$

where

$$u^*=\sqrt{\frac{\tau_w}{\rho}}\ . \tag{2.23}$$

The inner region of boundary layer can be divided in three sublayers (Viscous sublayer, Log-law layer, Buffer layer), as each layer has different flow characteristics as shown in Figure 6.

In the viscous sublayer, the fluid layer in contact with the wall is predominantly subjected to viscous effects and is usually laminar. However, in the log-law layer, the viscous and turbulent effects equally dominate the region [43].

Similar to this thesis, simulations that are relevant ignore wall-bounded effects. Also, separation is expected due to sharp changes in the geometry. That being said, the high y^+ wall treatment which lies in the log-law layer best represents for drag based turbines.

2.2.1 High y^+ Wall Treatment

The high y^+ wall treatment in STAR CCM+ is the equivalent to the stand wall function of $y^+ > 30$. This approach doesn't solve the viscous sublayer. Instead, the boundary conditions for the continuum equations are obtained by using the wall functions. The equilibrium turbulent boundary layer theory is used to derive wall shear stress, turbulent production, and turbulent dissipation. It is to be noted that the high y^+ wall treatment is the default in STAR CCM+ when the realizable k-epsilon model is used.

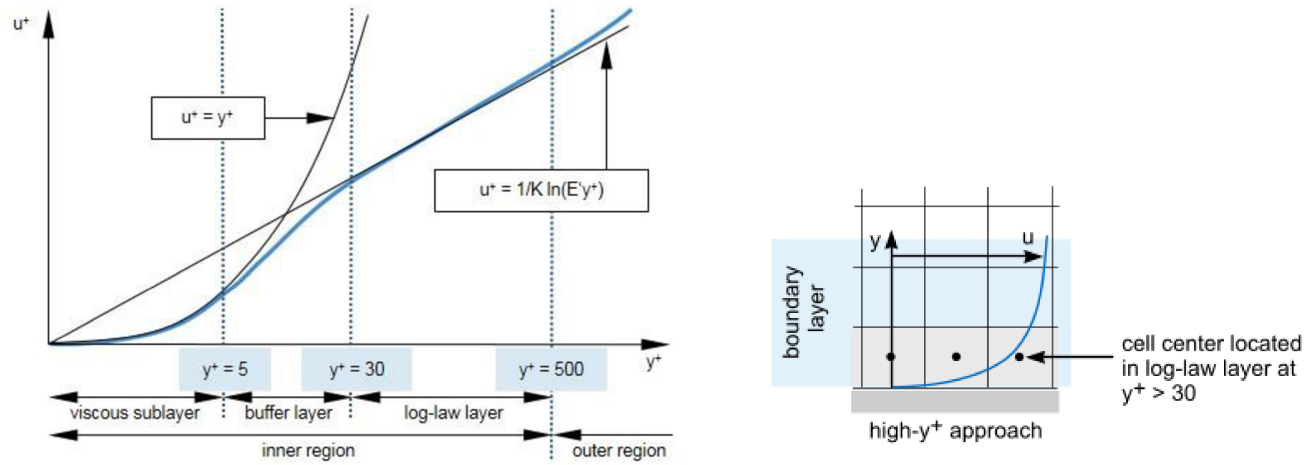

(a) (b)

Figure 6: Boundary layer Consideration, (a) Boundary layer sub-regions (b) High y^+ wall treatment [43].

2.3 Numerical Solver setup

The complex flow field over the evolved configuration of a building mounted seven bladed vertical axis Savonius turbine with a shroud, flange, and four guide vanes are numerically simulated by using a total grid of 10.85 million unstructured mesh elements, which consists of 1.659 million elements for the rotating rotor region, and 9.191 million elements for the stationary domain region including the deflectable vanes. Six different configurations of the vanes are studied and each case requires the construction of a different mesh. Air with a density of 1.1774 kg/m^3 and kinematic viscosity of $1.57x10^{-5}$ m^2/s is selected as fluid. This complex flow is solved by applying the realizable k-ε turbulence model to Unsteady Reynolds Averaged Navier Stokes (URANS) equations with the standard wall function approach of Y+> 30, on a no-slip boundary condition. The segregated flow model is used as it requires less storage and converges at a faster rate. As a beginning stage of the numerical simulation, implicit unsteady time steps with 2nd-order discretization are used for the calculation of the unsteady flow which is taken at 0.001 seconds. Calculations include 20 rotations of the turbine where a maximum number of 25 inner iterations are allowed to acquire convergence. It takes 4000-time steps to complete one rotation of the turbine, so for each time step Δt, the turbine rotates by 0.09°. It also important to note that each simulation took around 1 month.

2.3.1 Geometry of Turbine, Shroud, Building and The Far-Field Flow Region

The geometry of the turbine is taken from Krishnan et al. [37]. An isometric view of the geometry of the physical model that is used for the purpose of this study is illustrated in Figure 7. The computational domain is composed of two major regions, the stationary domain region and the rotating rotor region. The stationary domain region represents the far-field flow region, the building (shown as a square prism), shroud walls of the turbine, the flange, and the deflectable guide vanes. On the other hand, the rotor region contains only the seven blades and the rotor itself which is in rotation. A close up isometric view of the building and the system of shroud, flange,

and guide vanes which encloses the turbine, at the top of the building, is illustrated in Figure 7. The height and width of the building H' is 30.5 m.

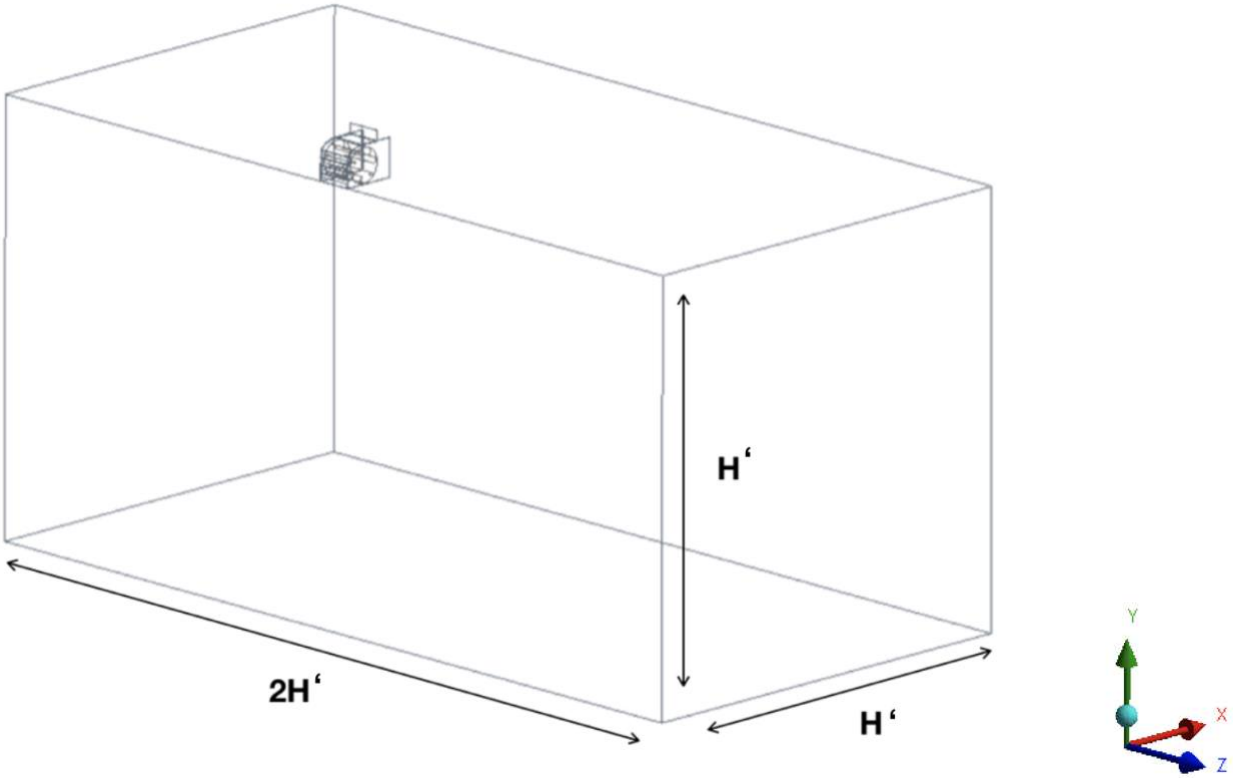

Figure 7: Close up view of the building and the roof mounted system of shroud, flange and guide vanes which encloses the turbine.

2.3.1.1 Geometry of the Guide Vanes

The main purpose of the deflectable guide vanes is to protect the wind turbine from hazardous weather conditions by blocking the entrance of the diffuser-shaped shroud. As a safety precaution, installation of the deflectable guide vanes controlled with a sensor mechanism enables the shroud to limit the inflow of the storm winds higher than 120 km/hr into the shroud. Otherwise, exposure of the rotating turbine to the inflowing wind at high speeds forces it to rotate at the angular speeds beyond the design limit, which could damage it. It is important to note the scope of this project was not to design a sensor mechanism.

The diameter of the rod was determined through simple fluid dynamics and stress analysis. Using the drag equation 2.24, the total amount of force can be found.

$$F = \frac{1}{2} C_D \rho V^2 A \tag{2.24}$$

The surface area (A) chosen for this case was taken to be the surface area when flow hits the guide vanes perpendicularly or when $\emptyset$ is 90 degrees (length x width). For worst case scenarios, the coefficient of drag was to be equal to 1, in which the case all flow approaching the plate comes to rest [44]. From the saffir-simpson hurricane wind scale category 1, storm speeds (V) of 120 km/hr were taken [45]. Finally, the max stress on the rod was to be determined [46]. The total load is taken to be distributed uniformly across the length of the rod.

$$\sigma = (yqL^2)/8I \tag{2.25}$$

where

$$I = \pi d^4/64 \tag{2.26}$$

For design purposes, by taking the minimum yield strength for steel ASTM-A36 (250 MPa) to be made equal to the maximum stress, the calculated diameter of the rod is 22.3 mm. Taking a design safety factor of 1.5 [47], the final minimum diameter of the rod that was taken into the design was 32 mm.

The profile of the guide vanes was designed for simplicity and to allow full closure of the shroud. For this reason, the said profile is made up of two convex circular arcs which are symmetrically joined together, across the maximum width of which an ASTM-A36 steel rod passes through, extending between the side-walls of the shroud.

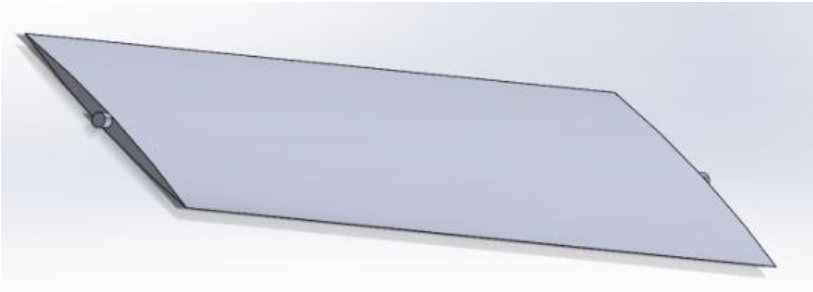

Figure 8: 3D CAD drawing of Guide Vane done in SolidWorks

The top view, side view, isometric view, and major dimensions of a guide vane are illustrated in Figure 9. The values of the major dimensions are given in the Table 2.

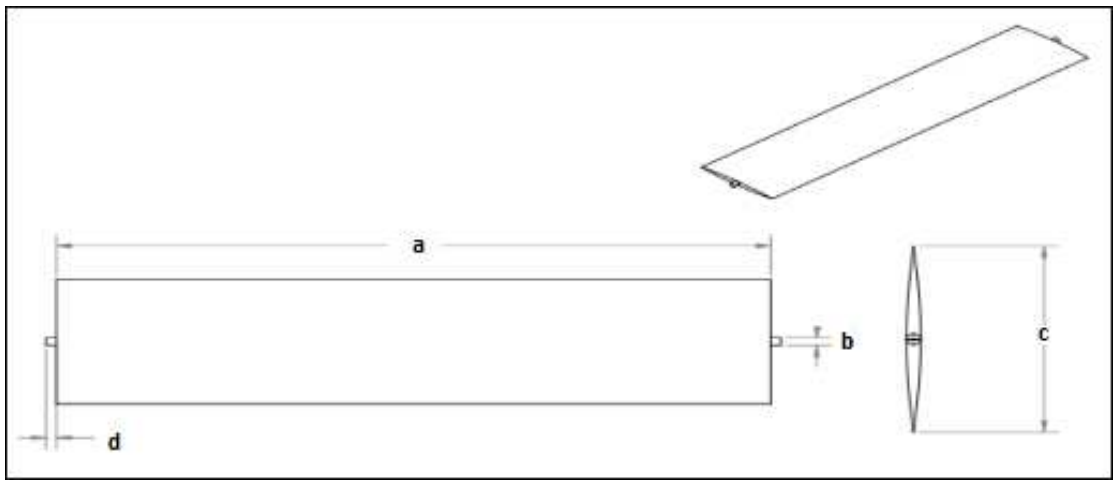

Figure 9: The top, side and isometric views and marked dimensions of a deflectable guide vane.

Dimension	a	b	c	d
Value	2450 mm	32 mm	550 mm	35 mm

Table 2: Values of the major dimensions of a vane

A side view of the final assembly drawing which shows the seven-bladed turbine enclosed in a shroud with a flange at the exit and four open deflectable guide vanes attached in the front is illustrated in Figure 10. Values of some of the major dimensions used in the analysis of the flow over rotating turbine, is tabulated in Table 3 in the form of non-dimensional parameters.

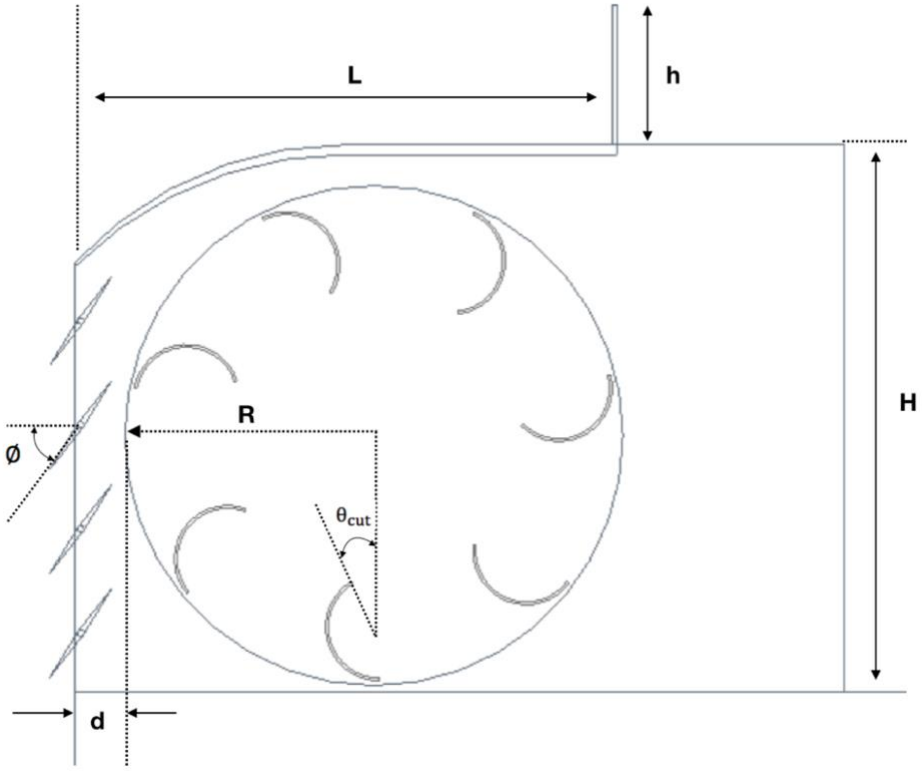

Figure 10: Side view of seven bladed turbine enclosed in a shroud with four deflectable guide vanes open that are attached in the front and a flange at the exit

Non-dimensional Parameter	$\frac{h}{H}$	$\frac{L}{H}$	ϑ_{cut}	$\frac{d}{R}$	$\emptyset$
Value	0.273	1	30^0	0.2	55^0

Table 3: Values of the some of the major dimensions in the form of non-dimensional parameters.

Three different cases were analyzed. The first one had all four guide vanes set at an angle $\emptyset$ of 35^0, 45^0, 55^0 or 65^0. The second study has the bottom two guide vanes closed at an angle of $\emptyset = 90^0$ and the rest of the vanes set at $\emptyset = 55^0$as shown in Figure 11(a). Similar to the second case, the last study has only the last vane set at an angle of $\emptyset = 90^0$ as seen in Figure 11(b).

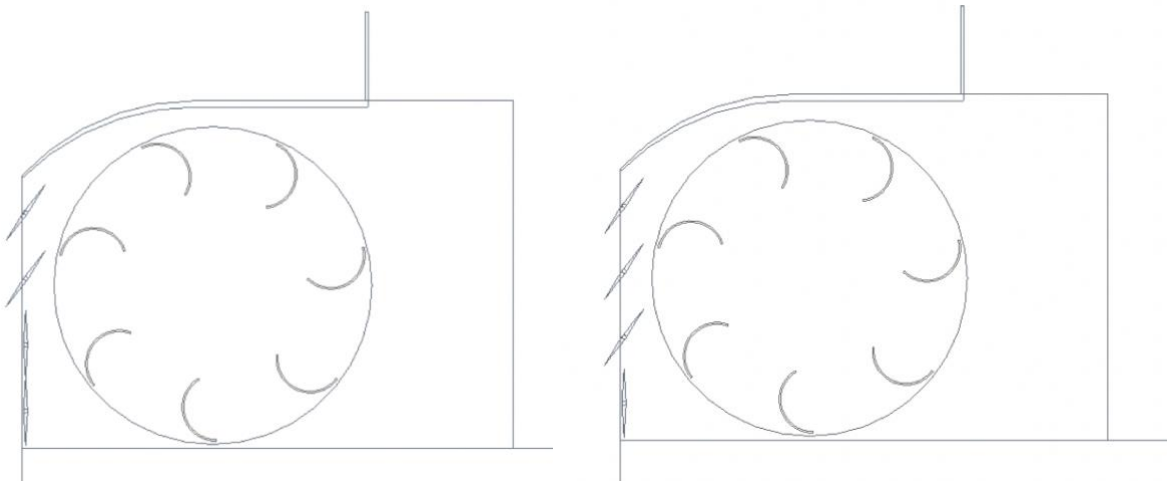

(a) (b)

Figure 11: Different configurations for the guide vanes (a) Bottom two guide vanes at $\emptyset = 90^0$, (b) Bottom vane at $\emptyset = 90^0$, and top 3 at $\emptyset = 55^0$ and top 2 at $\emptyset = 55^0$

2.3.2 Boundary Conditions

The different boundary types applied to the six surfaces of the combined computational domain of the stationary region and the rotating rotor region are briefly described in this subsection.

Figure 12 illustrates the full geometry of the computational domain. Figure 13 displays the domain region surfaces (without the walls of the turbine, shroud, flange and guide vanes) and their respective boundary types.

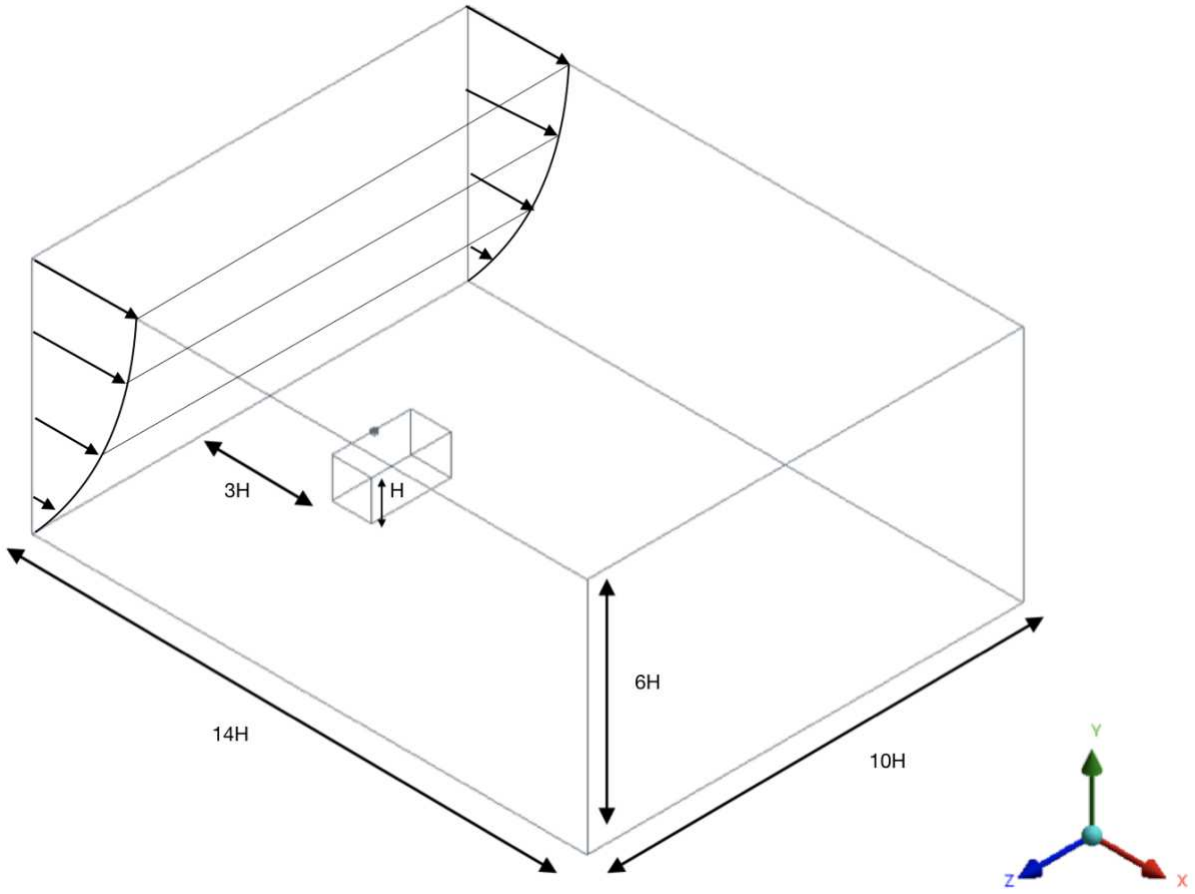

Figure 12: Numerical Domain Properties for 3D simulation with Building.

The no-slip boundary condition is applied to the walls of the building, the system of shroud, Flange, and guide vanes and the surfaces of the turbine blades. It is also applied to the whole bottom surface. The no-slip condition assumes that the air velocity at these solid surfaces is zero to simulate the effects of a solid wall boundary. The velocity inlet condition is applied at the upstream surface, in the form of atmospheric boundary layer (ABL) equation. Another velocity inlet condition is applied at the top surface of the domain region, in the form of a constant tangential velocity which is evaluated from the ABL equation and it is the same as the highest velocity at the upstream surface. The velocity profile is prescribed by Larin et al. [36] as shown in equation 2.27.

$$V_h = V_{top}(\frac{h}{H})^{0.31} \tag{2.27}$$

where V_h is the atmospheric boundary layer (ABL) velocity profile's variable speed, V_{top} is the velocity at a given height, h is the height measured from the ground and H is the height of the building. An exponent of 0.31 was used for urban settings. Figure 13 shows an isometric sketch of the velocity profile at the computational domain`s upstream (inlet) surface. The free stream velocity at the height of the turbine is defined as 3.89 m/s and the height of the building is taken as 30.5 m. taking these two values as constants in the equation shown above, the velocity profile can then be generated across the upstream surface.

These two boundaries of upstream and top surfaces simply serve as entry points for the fluid into the computational domain. The pressure outlet boundary condition is applied at the downstream (outlet) surface. Lastly, ABL velocity inlet boundary condition, in the form of a tangential component, is also applied both at the front and the rear surfaces of the domain.

It is also important to mention that a cylindrical internal interface boundary is created at the intersection between the stationary domain region's mesh and the rotating region's mesh, in order to separate the two different mesh regions.

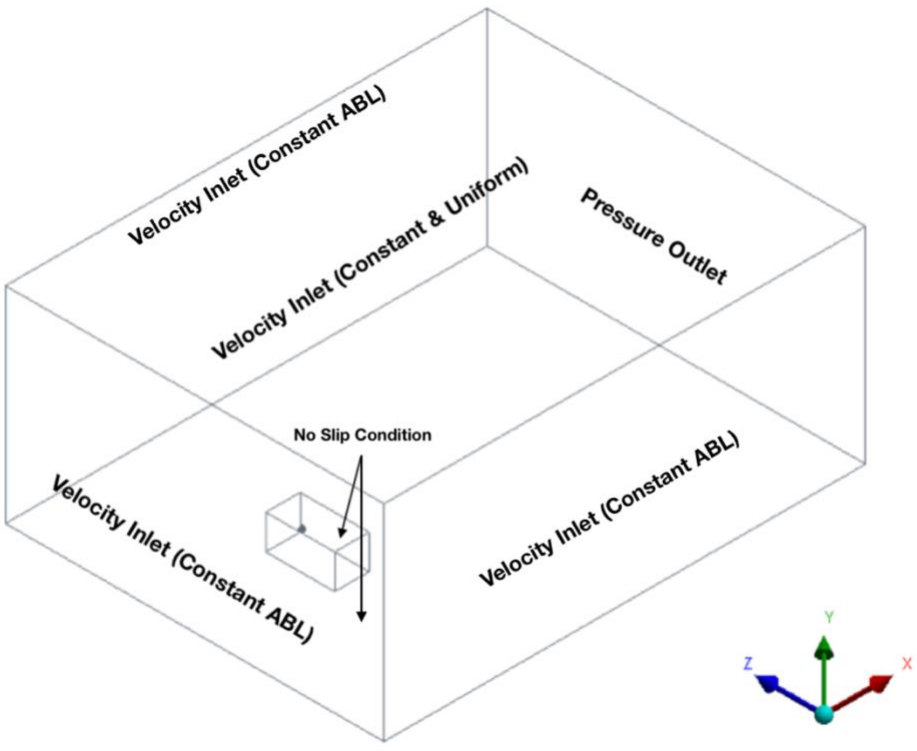

Figure 13: Boundary conditions applied to the computational domain (3D View)

2.3.3 Mesh Setup

Mesh element selection depends on the delivered accuracy, efficiency, and flexibility of the numerical solver. Polyhedral meshes have better accuracy than the tetrahedral meshes in three dimensional experiments [49]. Moreover, polyhedral meshes produced reduced element count, which is important because it minimizes computational cost. As well, the element quality (which measures mesh performance) of polyhedral elements is typically better than tetrahedral elements. One characteristic of polyhedral elements that might make them more cost effective is that they allow for a larger aspect ratio than triangular/tetrahedral cells. A large aspect ratio in a triangular/tetrahedral cell affects the skewness of the cell, which is unfavourable since it can affect accuracy and convergence. The latter is useful for simple geometries and consistent for convergence studies. Evidently, polyhedral elements are a better option.

Nevertheless, local refinement of a mesh is more challenging with polyhedral elements. Furthermore, tetrahedral elements are more adapted for complex geometries. They are advantageous because they reduce element count in areas of non-interest in the domain, as the elements can be made quite large. To leverage the advantages of both kinds of elements, an advanced layer mesher has been used for this simulation.

Advanced layer mesher generates a polygonal surface mesh from the initial triangulated surface, the prismatic cell layers are then generated by extruding the polygon surface in the region volume. This relaxes the dependency between the subsurface and region topology and allows the advanced layer mesher to generate a thicker layer with more uniform distribution. One of the key points of the advanced layer mesher is that it also collapses and splits faces and edges which helps to improve the mesh quality, in particular to help reduce self-skewness.

The quality of the mesh plays a big role in the accuracy of the computation, one of the attributes is the skewness. The skewness is classified as the difference between the shape of the cell and the shape of an equilateral cell of the same volume. As skewed cells with a high angle can decrease accuracy, triangular meshes should have all angles less than 85 degrees. Cells with a skewness angle above 85 degrees are considered bad cells [3]. In our design the skewness angle was less than 78 degrees.

Two different mesh regions are considered, the domain mesh region and the rotor mesh region. An interface was defined to split these two regions into a stationary and rotating mesh zone. They share the same geometrical properties than the regions mentioned in the model section of this thesis. Unstructured mesh cells were used for the entire domain and turbine, as structured mesh is not compatible for complex geometries unlike the unstructured mesh. In the area of interest, where the rotor mesh region lies, i.e. the rotating mesh area around the turbine blades, polyhedral elements have been used. In the domain surrounding the turbine casing and building, and the areas of the domain further from the building, tetrahedral elements have been used.

As elements to one side of the interface don't evidently match on the other side, the interface between the stationary(domain) and rotating (rotor) mesh create a non-conformal mesh. As shown in figure 15 and 16, the polyhedral elements in the area of interest (moving mesh) make a smooth transition to the domain region of tetrahedral elements.

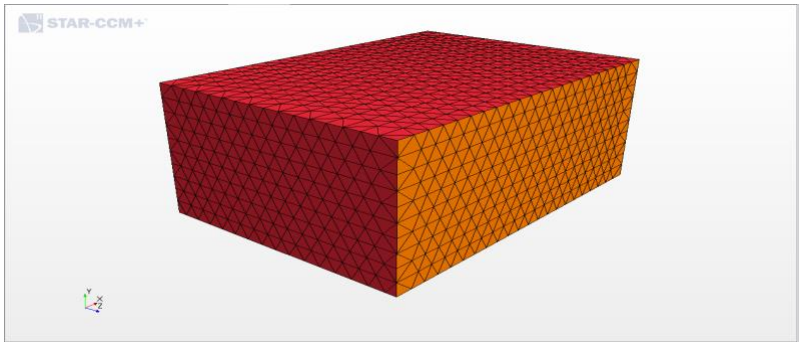

Figure 14: Tetrahedral Domain Mesh

Number of volume cells per region	
Domain mesh region	9,191,124
Rotor mesh region	1,659,215
Guide Vanes	501, 551
Total number of cells	10,850,339

Table 4: Number of volume cells per region

For areas of interest, mesh refinement was necessary in a couple of locations, the building and turbine mesh in the domain mesh region. As shown in the Figure 16, the domain mesh cells refinement increased with proximity to the rotor mesh region. This was done to improve the accuracy of the solution in those critical areas of the mesh. Furthermore, two spheres of influence were also used in front of the building and around the turbine. Volumetric controls were set on these two regions as shown in Figures 15 and 16.

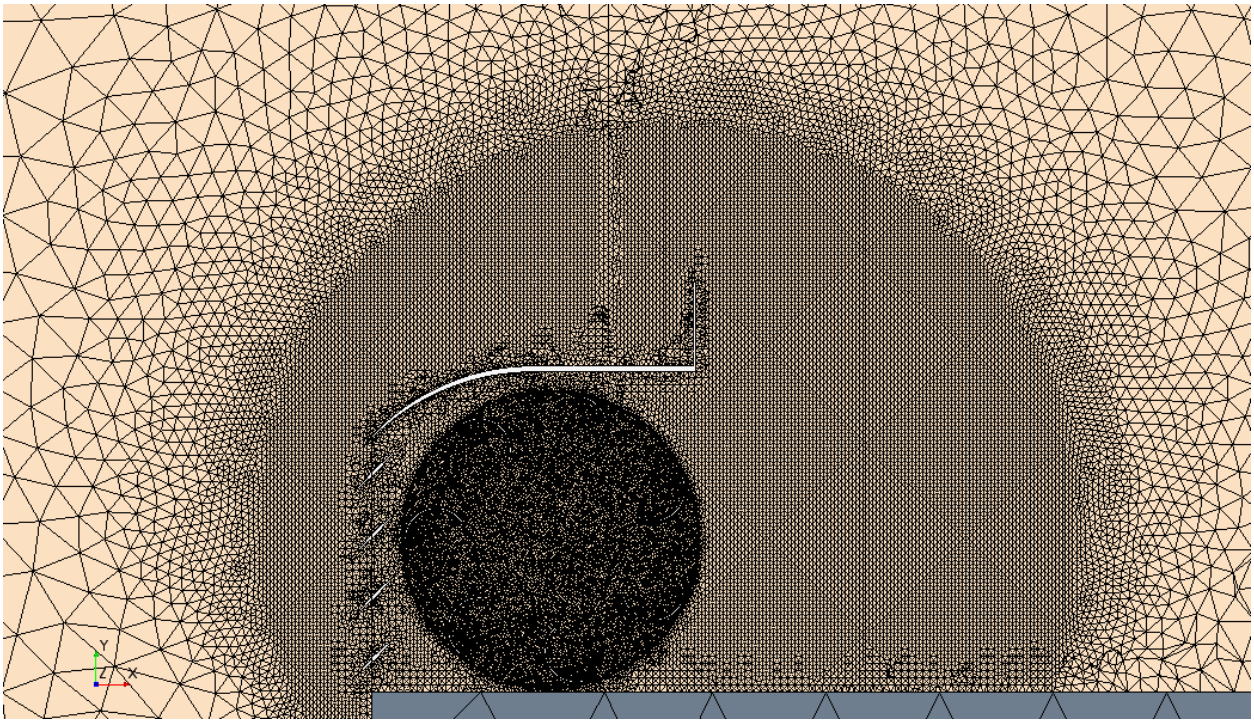

Figure 15: Close view of the turbines surface refinement and the shroud sphere of influence

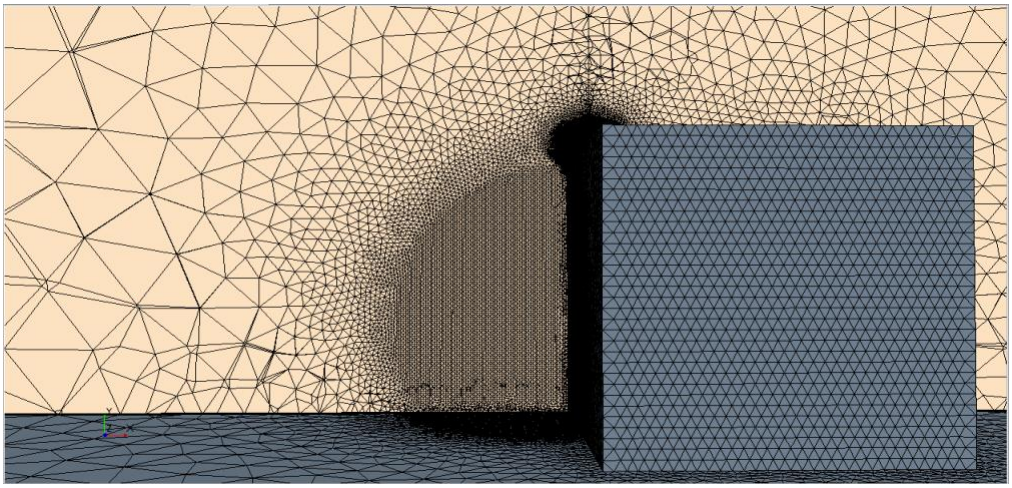

Figure 16: Close view of the building's surface refinement and the building front wall sphere of influence

For the stationary domain mesh region, a tetrahedral mesh was used with a base size value of 20m. The base size value is the reference length value for all size controls applied to the mesh. Also, the surface growth rate applied to all surfaces inside the domain mesh (except those affected by specific surface controls) is 1.2. The surface growth rate specifies the maximum size ratio of connected mesh edges for any surface. Furthermore, the volume growth rate applied to the domain mesh region cells is 1.1. This parameter dictates the cell size transition from the outer boundaries to the core mesh (which is the turbine mesh in this case). Surface controls were also added to certain surfaces to modify their refinement and generate the desired mesh. Numerical data for the volumetric and surface controls refinement inside the domain mesh region is further detailed in Table 5.

Volumetric and surface controls refinement data	
Surface controls	
Building's walls, Guide Vanes	Target surface size (in % of base size): 5% = 1m
	Surface growth rate: 1.1
Outer surfaces of the domain (top, front, rear, upstream, downstream and bottom)	Target surface size: 100% = 20m
Volumetric controls (spheres of influence)	
Building front wall sphere	Target cell size: 0.5m
Turbine sphere	Target cell size: 0.06m

Table 5: Volumetric and surface controls refinement data

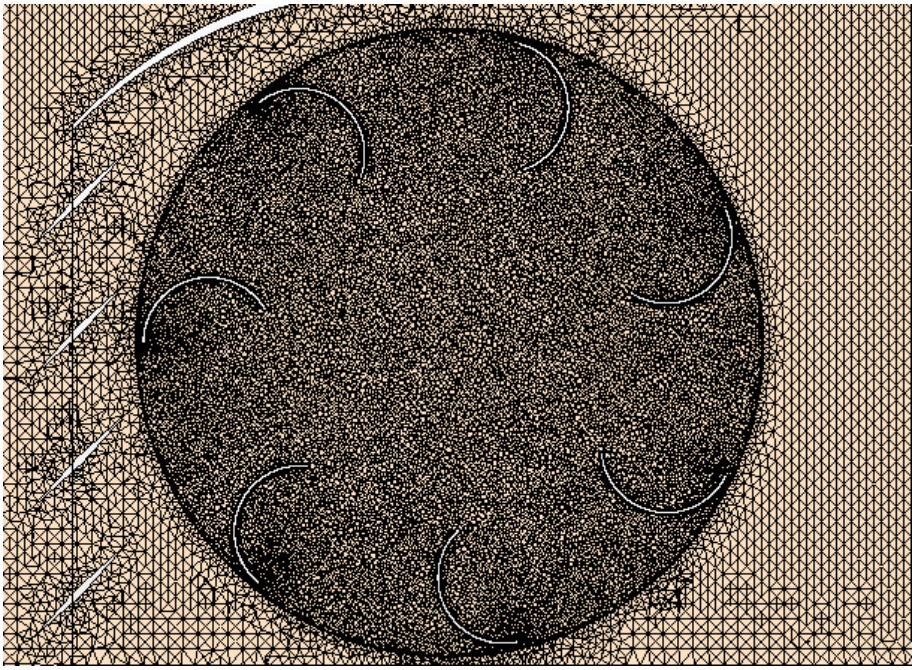

Figure 17: Rotor Mesh

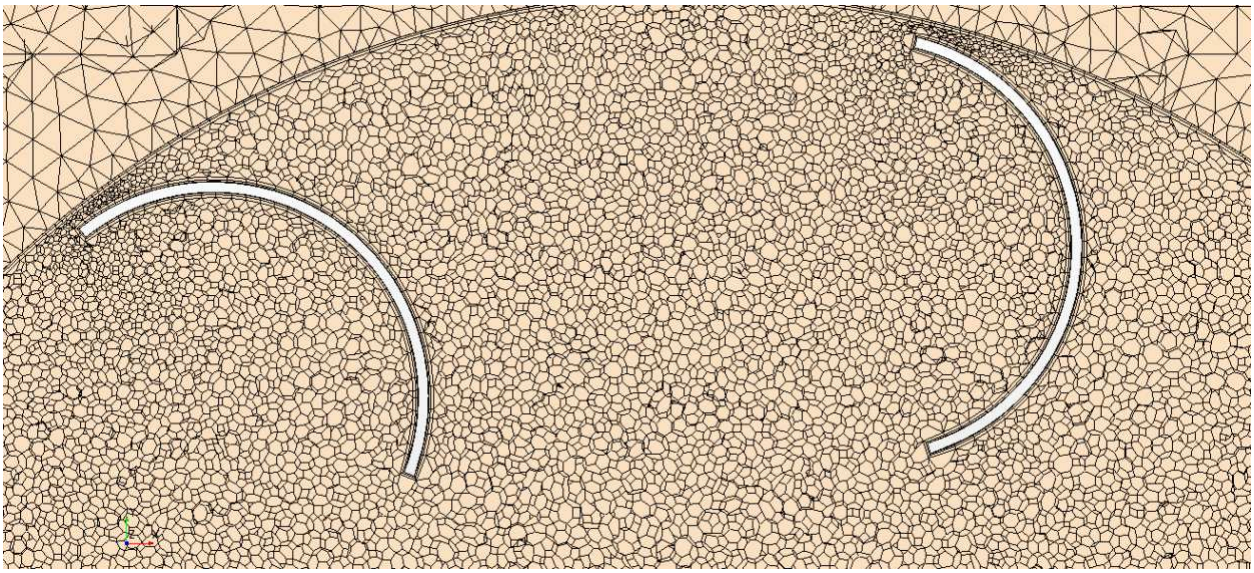

Figure 18: Polyhedral mesh around blade

For the rotating rotor mesh region, a polyhedral mesh approach was used with a base size value of 0.03m. The surface growth rate and volume growth rate values were respectively 1.1 and 1. Also, the mesh density parameter (number of cells over total region volume) of the rotor mesh region

was modified to increase the number of cells. It was changed from 1 to 1.5, considerably rising the number of cells inside the mesh while keeping their quality to an acceptable level. There are around. $6.85\ x10^3$ nodes set for each blade.

2.3.4 Grid Verification

To verify our methodology, a grid verification study has to be performed. The purpose of this study is to guarantee that the refinement of the grid doesn't affect the results significantly. A reduction factor is used to gradually refine the grid until the difference in the results is reasonably small. At a TSR of 0.5 and a reduction factor of 1.35, the flow in fine and finer grids are simulated. These results are shown in a coefficient of moment versus rotational angle graph in Figure 19 and summarized in Table 4.

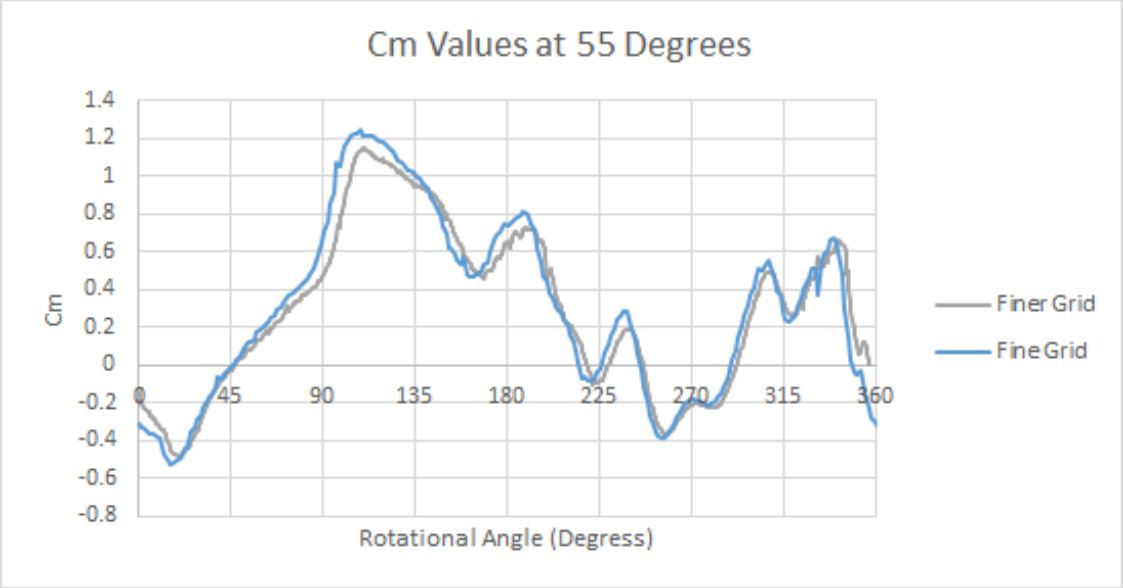

Figure 19: Comparison of the variation of the moment coefficients C_m of blade 1 of the turbine throughout its rotation of 360° with guide vanes all open and set at 55°, for finer mesh and finer grid.

	Refinement	
	Fine Grid	**Finer Grid**
Number of Elements (10^6)	10.85	13.67
Base Size Rotor Region	0.04	0.03
Cp Value	0.333	0.336
Cp Difference	0.9%	
y^+	30	
Size Reduction Factor	1.35	
Growth Rate	1.1	
Convergence Criterion	1.0E-5	

Table 6: Dependence of the power coefficient C_p upon grid refinement.

As Table 6 verifies that with grid refinement, the difference of C_p values between the fine and finer grids have very similar values. In order to save computational time, the coarse grid is used for the design analysis.

2.3.5 Convergence Criteria

The power coefficient convergence for each guide vane angle required a certain numbers of cycles to converge. The power convergence is shown in figure 20 for TSR 0.5. The graph illustrates the importance of simulating multiple cycle to gain stable results, and to not obtain an over prediction in the Cp values when simulating insufficient amounts of cycles.

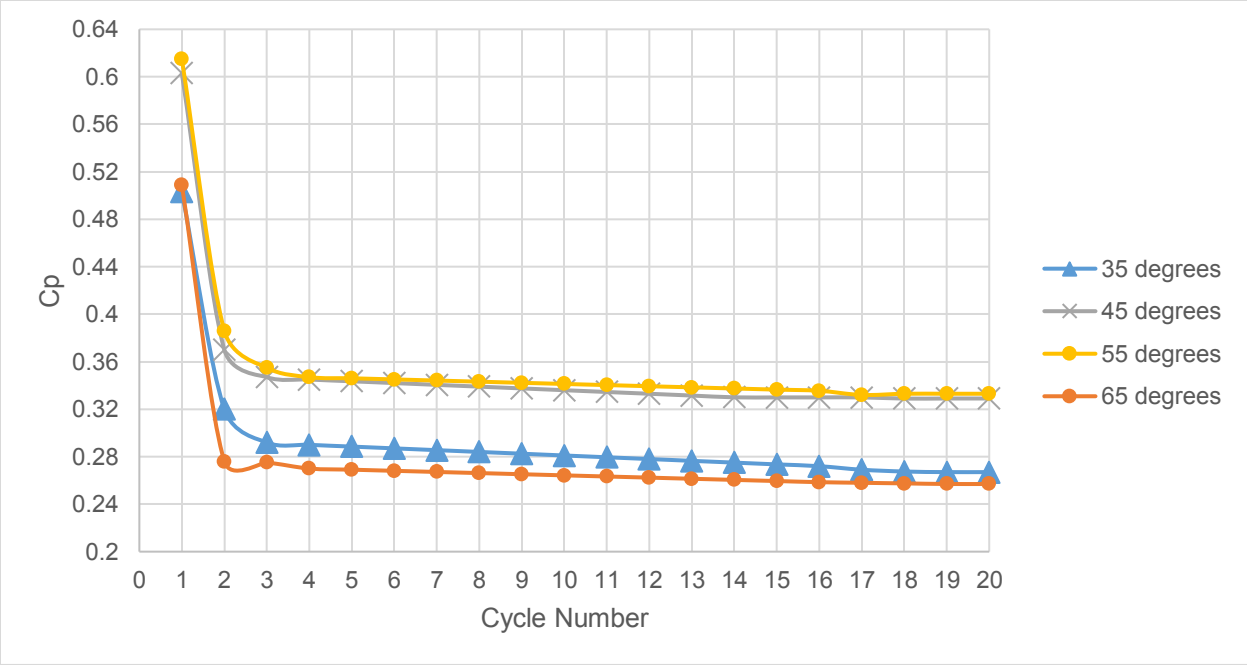

Figure 20: Cp Convergence for Different Guide Vane Angles at TSR = 0.5 to 20 cycles.

The power coefficient convergence for guide vane angle of 45 and 55 degrees had the fastest convergence relative to the number of cycles, converging around 12-14 cycles. While the angles of 35 and 65 degrees needed 14-16 cycles to converge. The criterion chosen for each simulation to reach satisfactory convergence was at most a one percent difference of Cp values from the last four cycles. The average power coefficient value was taken from the last two revolutions for each case.

CHAPTER 3: RESULTS & DISCUSSION

3.1 Moment Coefficient of the Blade

The moment coefficient C_m is calculated for the last rotation of one blade as a function of rotation angle. The rotation angle Ω is measured in clockwise direction starting from downward vertical line (6 o'clock position) as shown in Figure 21. In Figure 22, variations of the moment coefficients are shown for the time steps (0.001 s and 0.0005 s) throughout 360° rotation, for the flow with a TSR of 0.5 and with guide vanes set at 55°. It is obvious that the C_m curves for both time steps are close and similar and this fact justifies the use of the larger time step of 0.001s as it is computationally faster.

3.2 Guide Vanes Parameter Study

First, results for the flow over and through the seven-bladed wind turbine enclosed inside a diffuser-shaped shroud with four deflectable guide vanes, set at an entrance angle of 45° with respect to the horizontal direction are presented in a straight wind direction. Mid-plane pressure colors as well as mid-plane velocity colors of the flow in the wind direction are illustrated in Figures 24 and 27, respectively. Secondly, power coefficients (C_p) of the turbine with guide vanes for the flows at three different vane angles of 35°, 45°, 55° and 65° respectively, and at a tip speed ratio of 0.5, are calculated. These angles were selected based on the research of roof top flow by Larin and Paraschivoiu [36] as it was shown that the flow passing on the edge of roof was around the angle of 45°. Thus, angles around 45° were conducted to validate the most effective vane angle for power generation. These results are as shown in Table 7. Lastly, power coefficients (C_p) of the turbine without guide vanes for the flows at tip speed ratios of 0.38 and 0.5, calculated by Krishnan and Paraschivoiu [37] are as shown in Table 8.

It is concluded that the most efficient flow of the turbine with the vanes can be achieved at a vane angle of 55°. Hence, the highest power coefficient is 0.333, which is lower than the C_p value 0.394 for the turbine without guide vanes, at the same TSR (0.5) by 15%.

Vane angle	Maximum C_p Value
35°	0.267
45°	0.329
55°	0.333
65°	0.259

Table 7: Turbine power coefficients at different guide vanes angles, at TSR 0.5.

TSR	C_p Value
0.38	0.340
0.5	0.394

Table 8: Turbine power coefficients with no guide vanes, at TSRs 0.38 and 0.5 [37].

3.2.1 Blade Analysis

For the analysis of the rotation of blade 1, the following observation can be made. In Figure 23, the guide vanes are deflected at 45°, TSR is set at 0.5 and the time step is taken as 0.001 s. As the blade 1 starts its rotation from zero-degree position of the rotational angle Ω (six o'clock position), the blade receives little incoming flow since it is shielded by the edge of the top of the building and also by the deflected guide vanes. Once it passes this shielded region about 30°, concave side of the blade 1 starts being gradually exposed to the inflow, and it starts to generate positive torque in a drag-based fashion, passes from 90° (Figure 23) and attains its maximum value about 120°. After 120°, a part of the inflow starts by-passing concave side of the rotating blade and this part of inflow tends to flow on the convex side, thus causing the positive values of the torque to decline up to 270°. Starting from 270° (Figure 24) up to 330°, another branch of the inflow starts filling into the concave side of the rotating blade, thus causing the positive torque to increase again. However, starting from 330° on, the upstream flow starts making a major effect on this blade, as a result, the flow accelerates over the concave side of the blade. Thus, upstream flow starts to generate lift on the blade which is caused by an important pressure drop on the concave side and this affects the results in diminishing or negative torque values for the rest of the rotation up to the 360°. Torque generation characteristic of the first blades of the similar designs of the multi-bladed

Savonius turbines during a 360° rotation should be expected to display similar patterns. Thus, a similar torque generation pattern is repeated both in Figure 22 and 25.

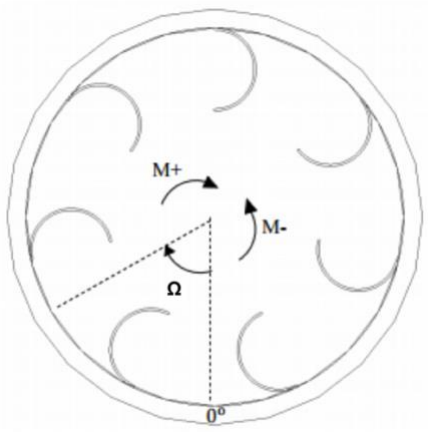

Figure 21: Rotational angle convention and position

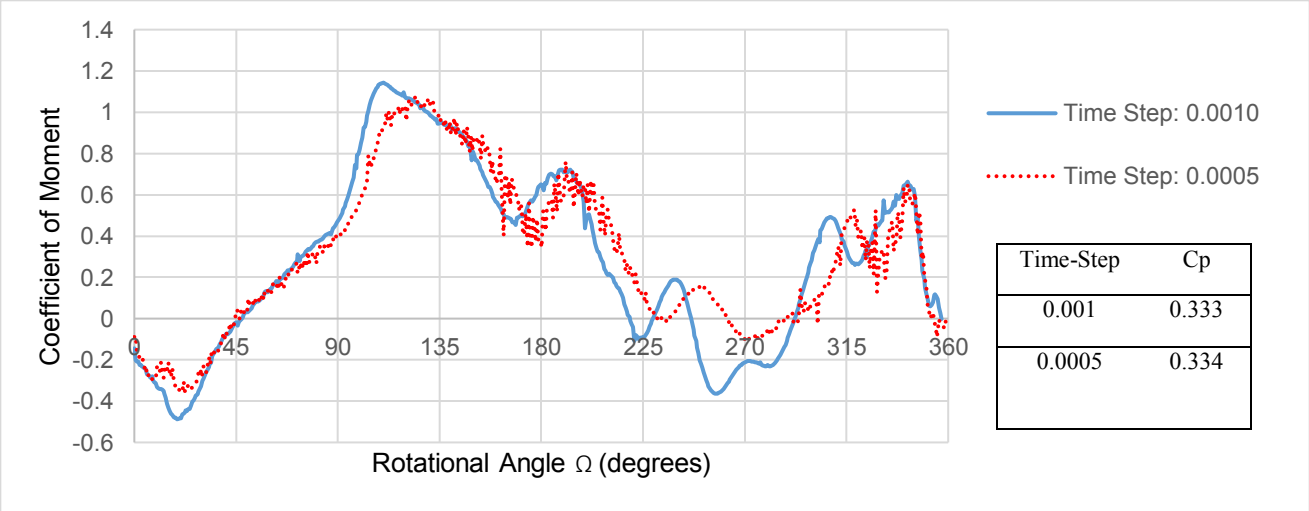

Figure 22: Comparison of the variation of the moment coefficients C_m of blade 1 of the turbine throughout its rotation of 360° with guide vanes all open and set at 55°, for time steps of 0.0010 s and 0.0005

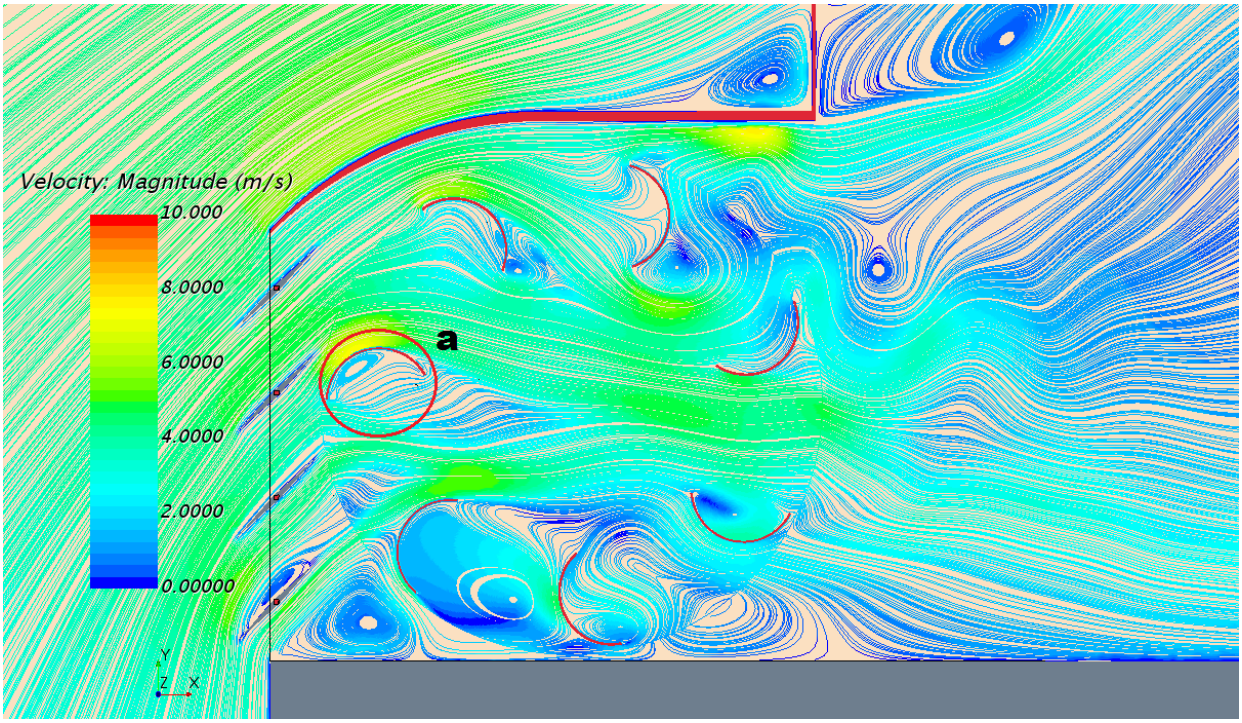

Figure 23: Mid-plane velocity colors and streamlines of the straight wind flow entering the shroud of seven bladed turbine, with blade 1 (encircled) rotated 90°, through 45° guide vanes.

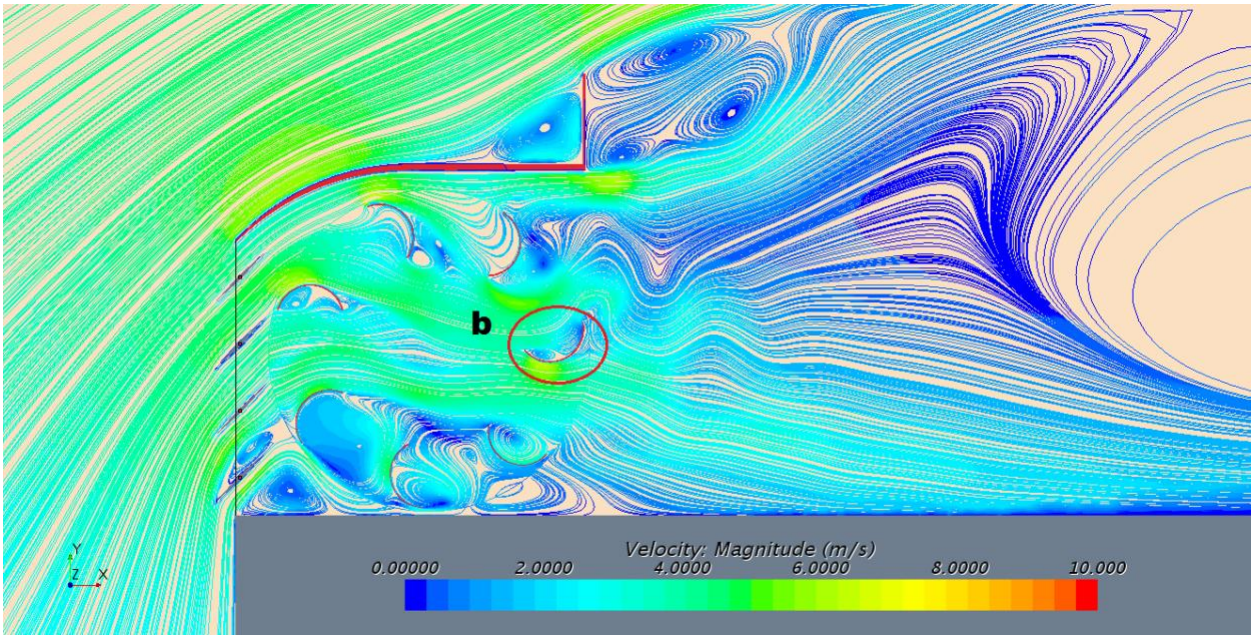

Figure 24: Mid-plane velocity colors and streamlines of the straight wind flow entering the shroud of seven bladed turbine, with blade 1 (encircled) rotated 270°, through 45° guide vanes.

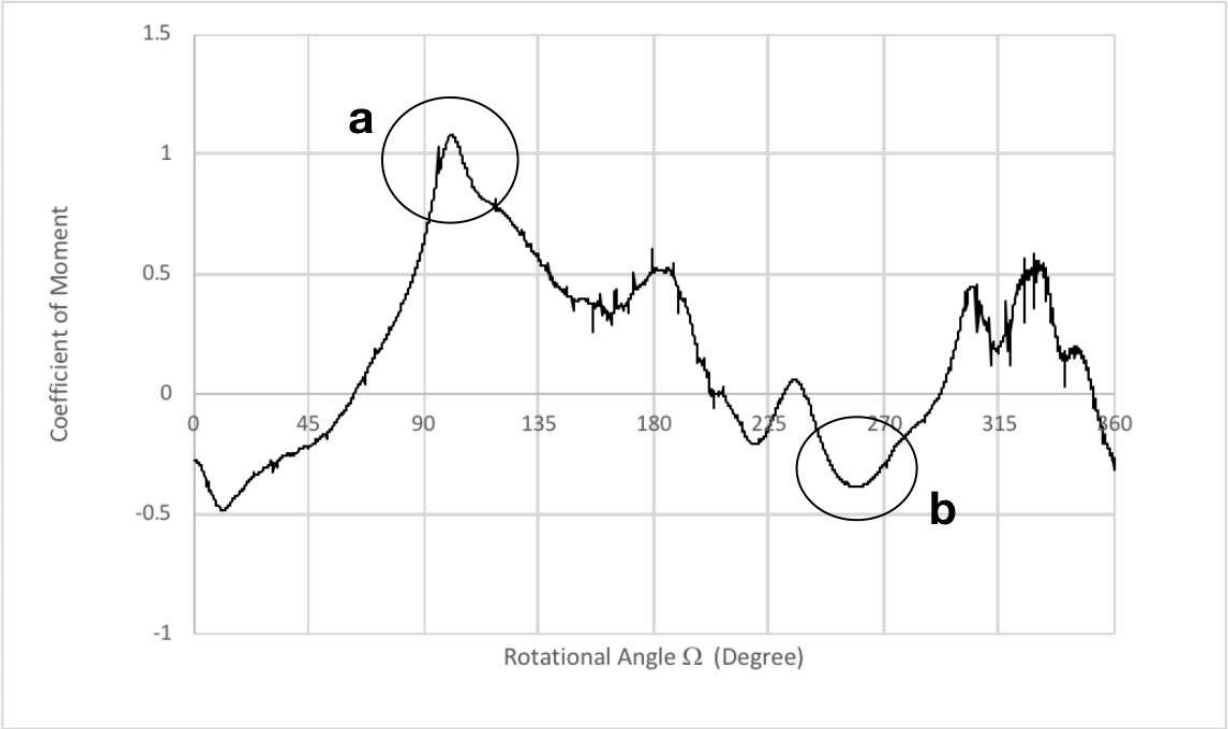

Figure 25: Moment coefficients C_m of blade 1 of the turbine throughout its rotation of 360° with guide vanes all open and set at 45°, for TSR 0.5.

At a tip speed ratio of 0.5, the coefficient of moment of blade 1 with guide vane angle set at 55° are compared individually with vane angle 35°, 45° and 65° in figure 26, 30, 33 respectively. Despite Figure 26, Figure 30 and 33 represent similar patterns in the torque generation to blade 1, the upstream flow for the 35° vane angle shown in Figure 26, begins to generate positive torque at rotational angle of 0° in comparison to rotational angle of 45° for the other three guide vane angle as shown in Figure 30 and 33. This phenomenon might be due to the obstruction the 35° vane angle causes to the incoming wind flow.

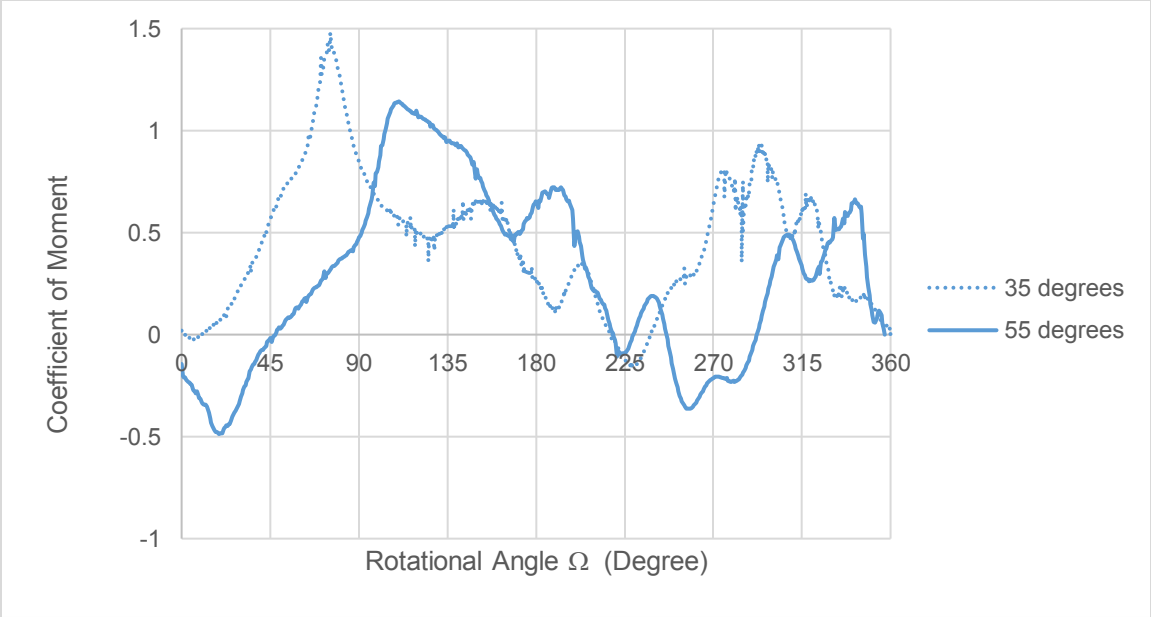

Figure 26: Comparison of moment coefficients C_m of blade 1 of the turbine throughout its rotation of 360° with guide vanes angles of 35° and 55°, for TSR 0.5.

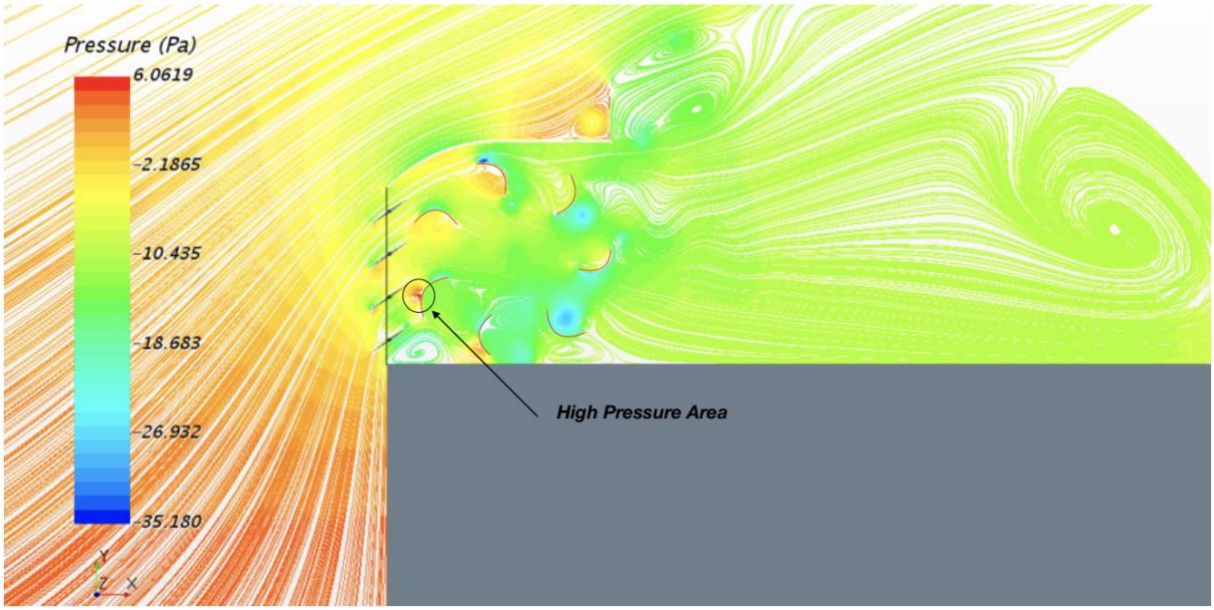

Figure 27: Mid-plane pressure colors and streamlines of the straight wind flow entering the shroud of seven bladed turbine, through 35 ° guide vanes. Note the region of high pressure encircled after the guide vanes.

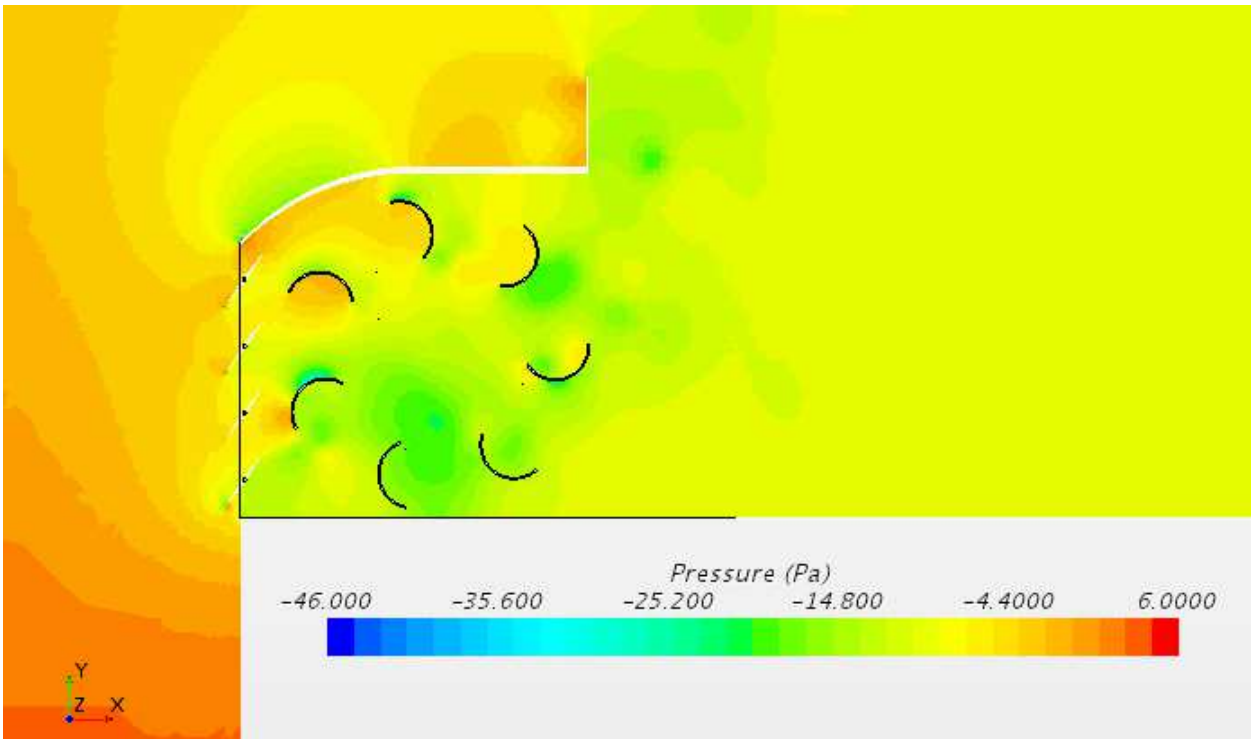

Figure 28: Mid-plane pressure colors and streamlines of the straight wind flow entering the shroud of seven bladed turbine, through 55 ° guide vanes.

The pressure colors displayed from the results may explain the differences in the C_p values in Table 7. As illustrated in Figure 27, the mid-plane pressure colors of the flow in the straight wind direction through 35° guide vanes form a region of high pressure as encircled near the guide vanes. As it is being partially interfered by the guide vanes, only the 35° flow seems to be affected when its pressure colors and streamlines (Figure 27) are compared to the pressure colors of the flows through the guide vanes 45° and 55° (Figure 31 and Fig. 28, respectively).

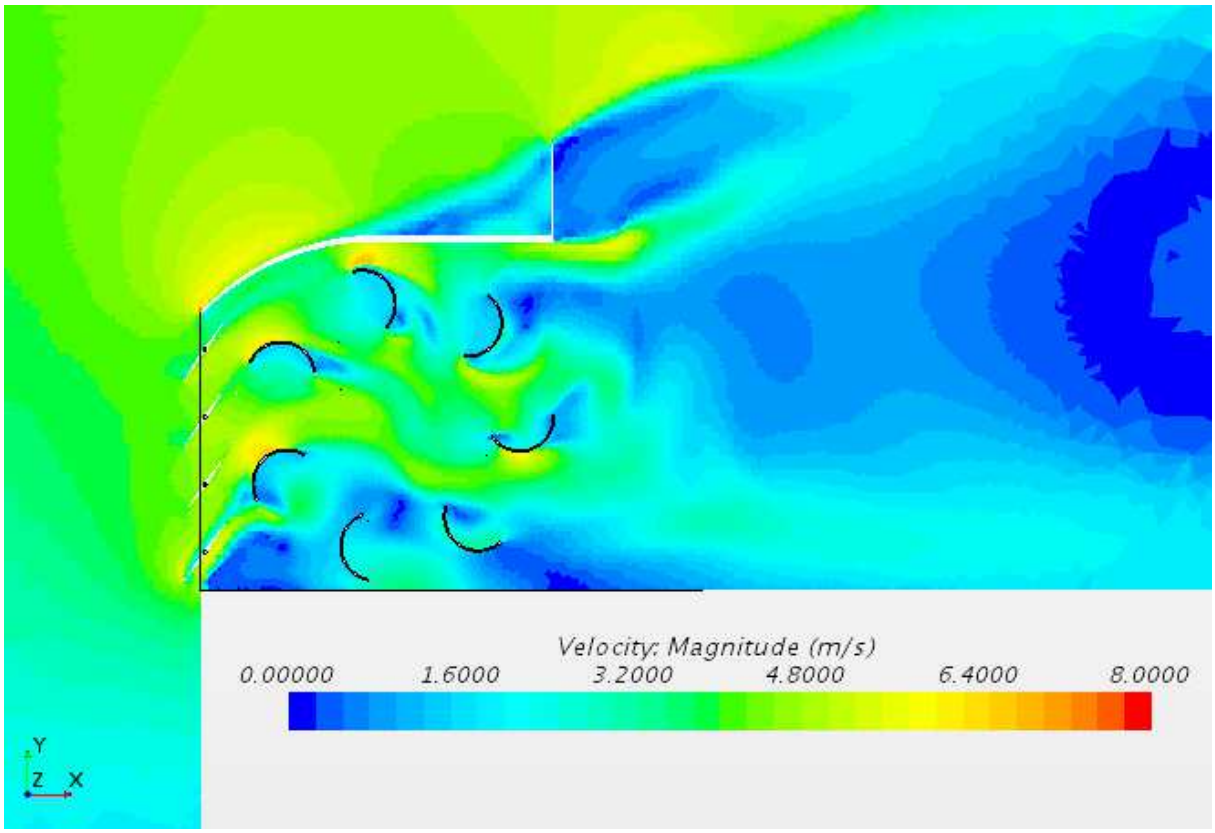

Figure 29:Mid-plane velocity colors of the straight wind flow entering the shroud of seven bladed turbine, through 55° guide vanes.

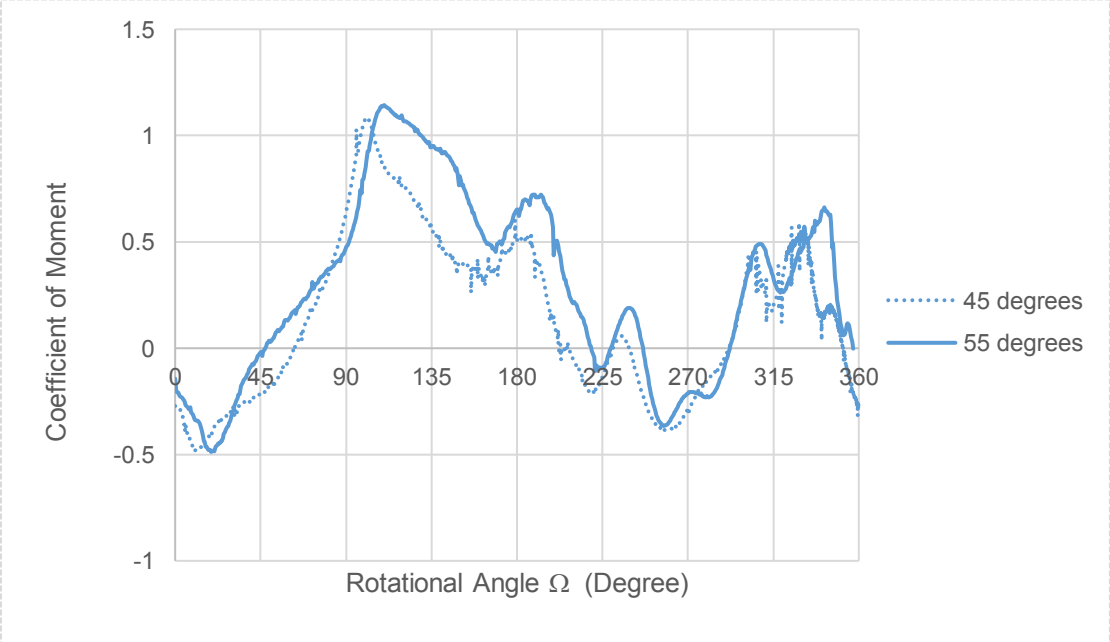

Figure 30: Comparison of moment coefficients C_m of blade 1 of the turbine throughout its rotation of 360° with guide vanes angles of 45° and 55°, for TSR 0.5.

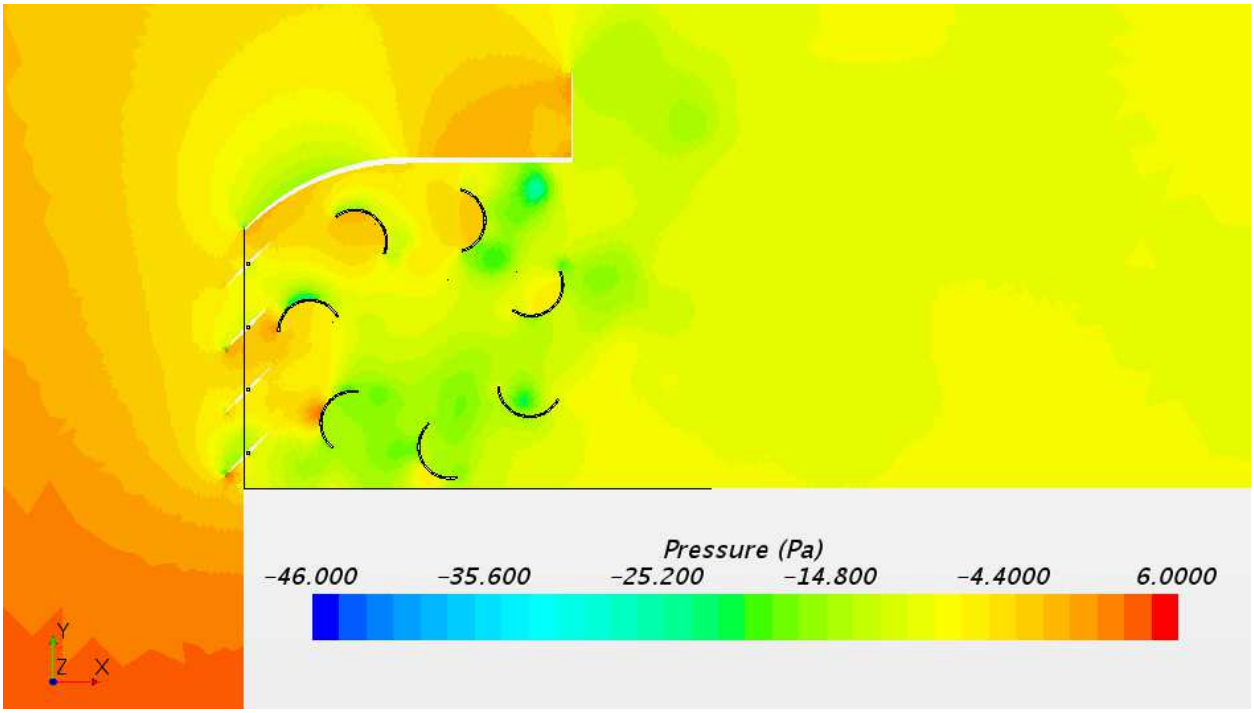

Figure 31: Mid-plane pressure colors of the straight wind flow entering the shroud of seven bladed turbine, through 45 ° guide vanes.

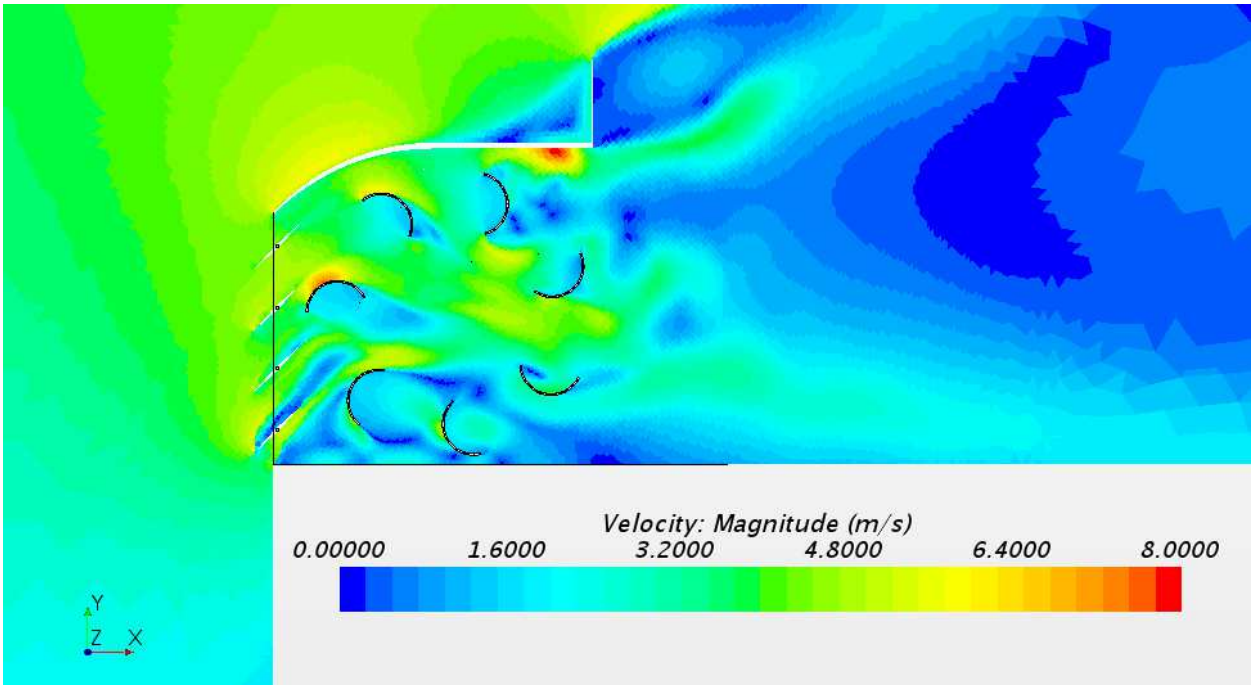

Figure 32: Mid-plane velocity colors of the straight wind flow entering the shroud of seven bladed turbine, through 45° guide vanes.

Another factor to the differences may be due to the vortices behind the flange. The strong vortices create a low-pressure region and are responsible for the increase in mass flow of wind into the turbine, for each case of the flow through guide vanes. However, it is important to note that the size of these vortices does not solely depend on the performance of the turbine. As illustrated from the comparison of the Figures 31 and 28, for the flows through angles 45° and 55°, respectively, the flow through angle 55° which forms a stronger vortex behind the flange creating a lower pressure zone, has a higher C_p value.

Furthermore, in Figure 30, the difference in the coefficient of moment at rotational angles of 90° to 180° can be explained in the pressure colors illustrated in Figures 28 and 31. The upstream flow for guide vanes angle 40° (Figure 31) starting at rotational angle 90° seems to have a higher-pressure zone than guide vane angle 55° at that location (Figure 28).

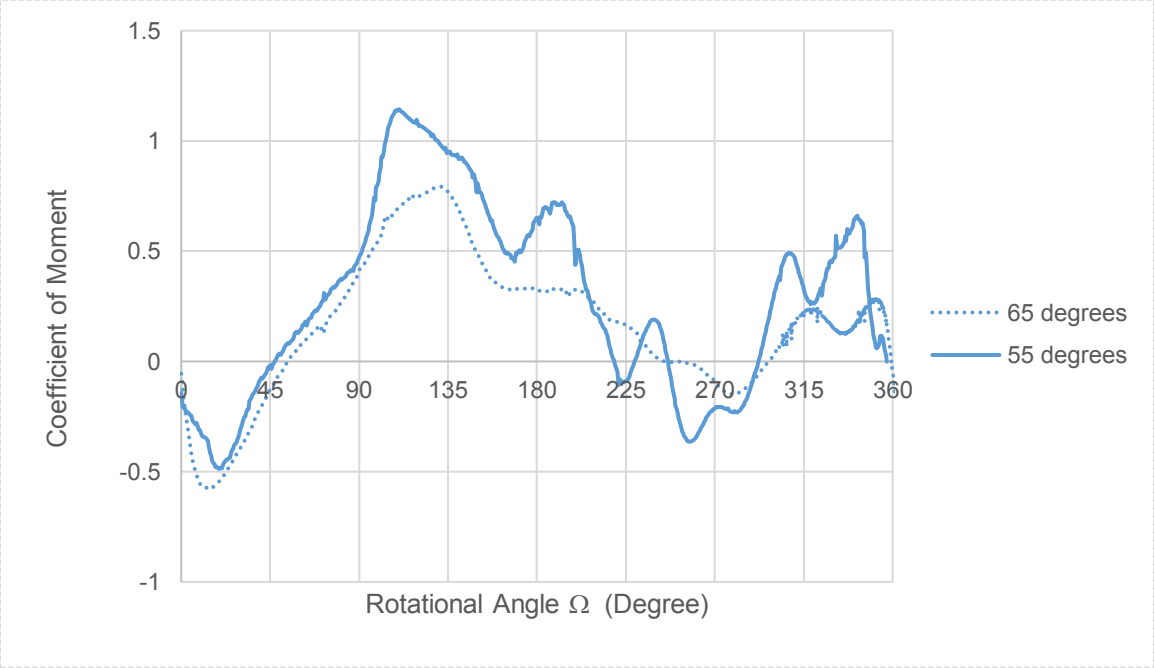

Figure 33: Comparison of moment coefficients C_m of blade 1 of the turbine throughout its rotation of 360° with guide vanes angles of 55° and 65°, for TSR 0.5.

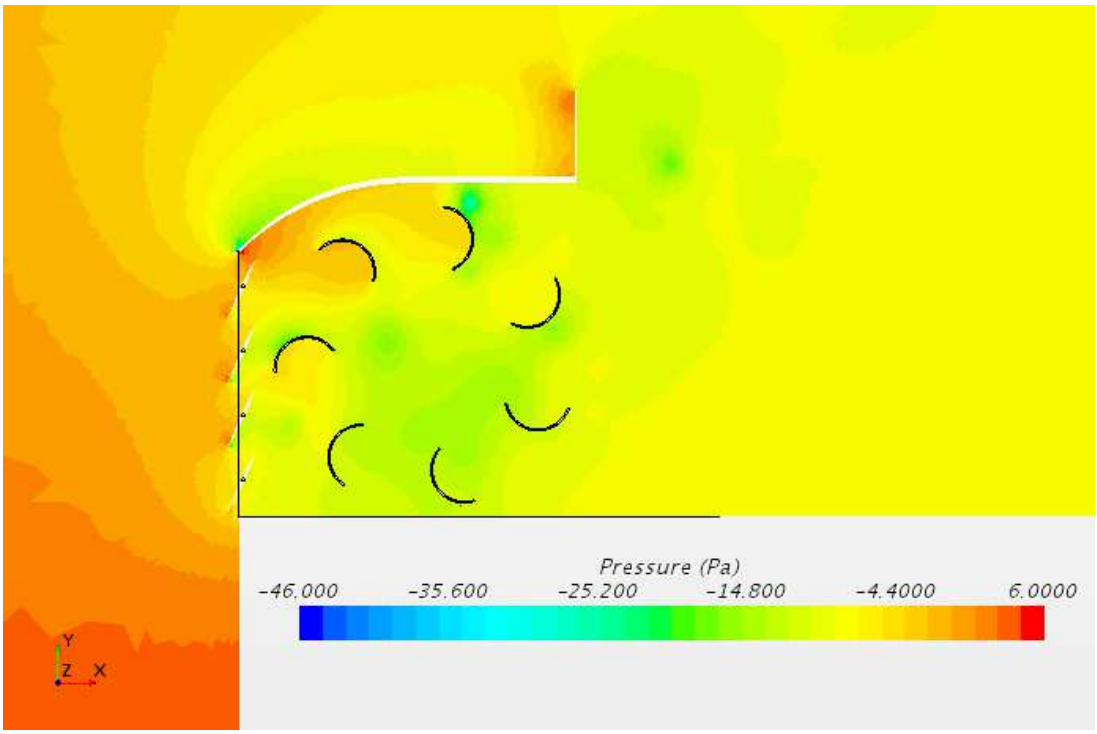

Figure 34: Mid-plane pressure colors of the straight wind flow entering the shroud of seven bladed turbine, through 65 ° guide vanes.

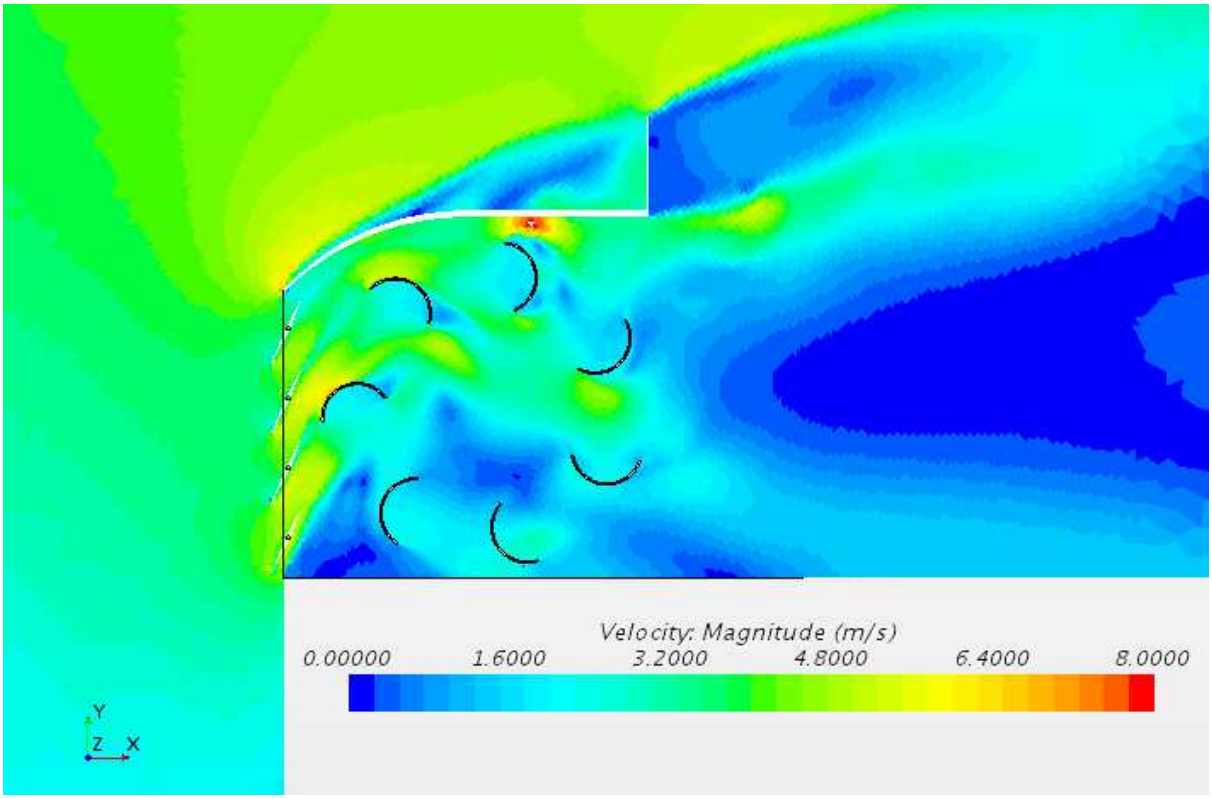

Figure 35: Mid-plane velocity colors of the straight wind flow entering the shroud of seven bladed turbine, through 65 ° guide vanes.

The Cp difference between guide vane angle 55° and 65° is well illustrated in Figure 33. Figures 29 and 35 provide a difference as the flow going through the turbine is very minimal at guide vane angle of 65° (Figure 35) compared to guide vane angle of 55° (Figure 29).

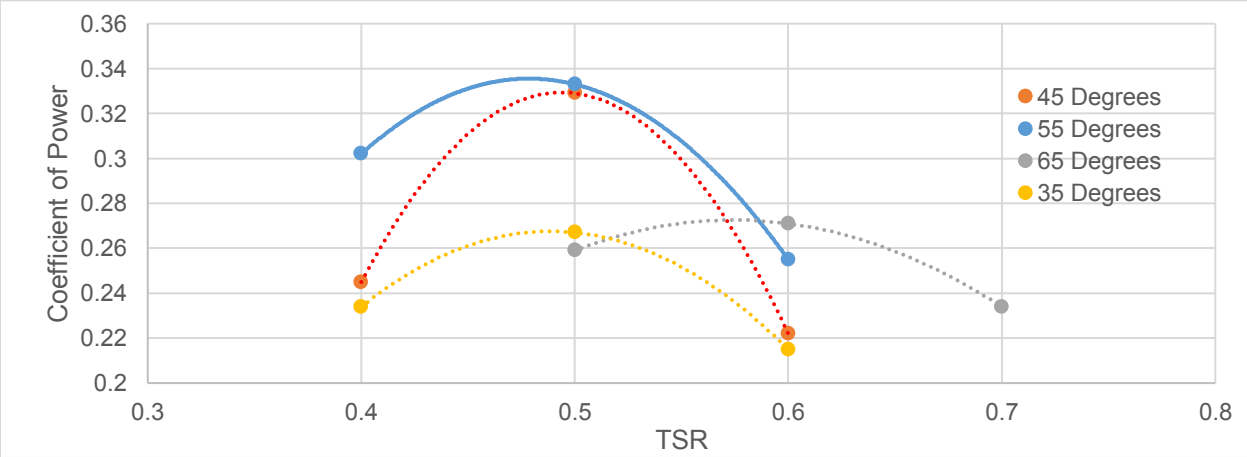

Figure 36: Coefficient of Power Summary for guide vane angles of 35°, 45°, 55°, and 65 °

The modification of the guide vane angles not only changes the torque profile, but also changes the peak power. The lines shown in Figure 36 are quadratic curves representing the calculated coefficient of power for each case. In Figure 36, it is clear that an increase in the guide vane angle only till guide vane angle of 55° results in an increase in peak power and a reduction of the TSR value when this peak value is obtained.

It is to be noted that although the guide vane angle of 65° has the highest peak at TSR of 0.6, guide vane angles of 35°, 45° and 55° show better performance at lower TSR values. This difference should be considered when safety precautions are taken during storm winds. As the peaks of the Cp curves differ with respect to the change of the guide vane angle, it is important to simulate a range of TSR values to overcome the understanding of the results.

3.2.2 Closed Guide Vanes

Two additional studies were analysed with the idea of deflecting the flow directly to the upstream blade as the region of rotational angle 0° to 45° does not generate power effectively as shown in Figure 37. This figure also shows that the flow is hitting the convex side of blade 2 which causes a negative torque.

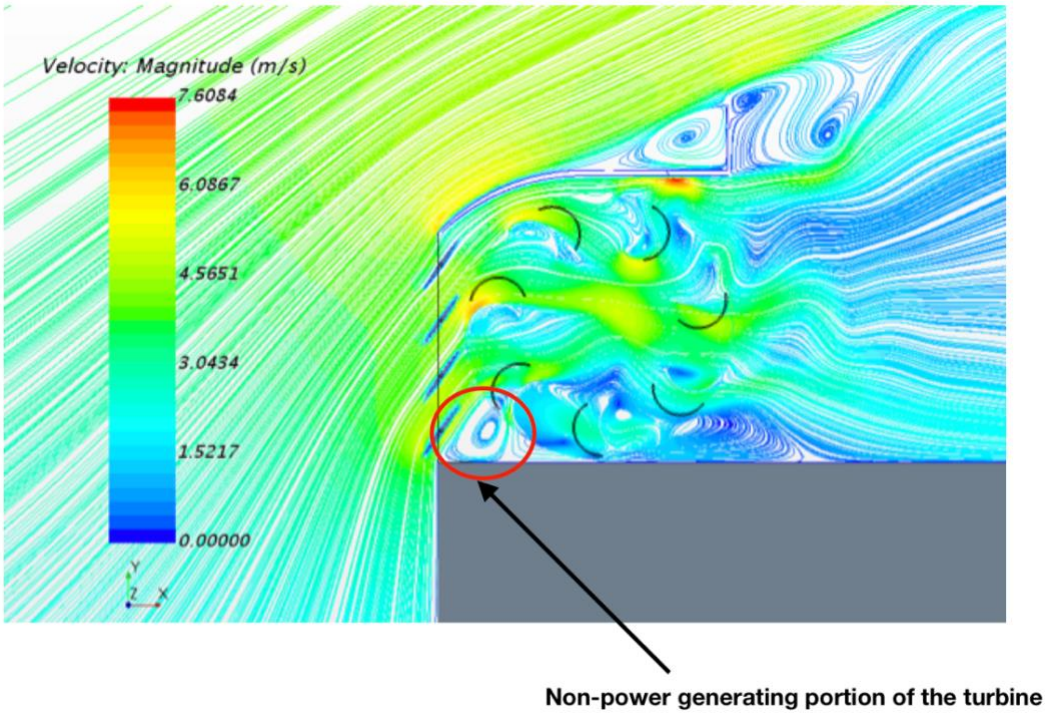

Figure 37: Mid-plane velocity colors of seven bladed turbine, through 55° guide vanes all open.

Case Study	Cp value	% difference from guide vane 55° Cp (0.333)
Case 1	0.109	67.3 %
Case 2	0.398	19.5 %

Table 9: Turbine power coefficients for different cases for guide vane angle 55°, at TSR 0.5.

Using the baseline with guide vane angle of 55° at TSR 0.5 which had the highest Cp value, the first study (case 1) was to have the bottom two guide vanes closed at an angle of $\emptyset = \mathbf{90^0}$ and the rest of the vanes set at $\emptyset = \mathbf{55^0}$. It was concluded that this geometry was ineffective as hardly any wind flow passed through the turbine as shown in Figure 38 and 39. This case had a Cp value of 0.109 and a 67% difference compared to the highest Cp at guide vane $\emptyset = \mathbf{55^0}$.

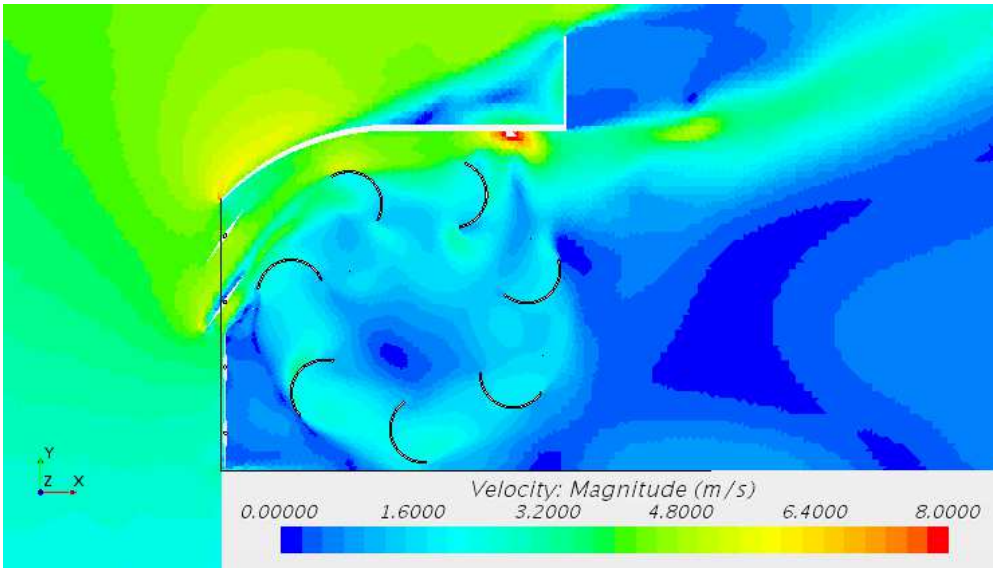

Figure 38: Mid-plane velocity colors of seven bladed turbine, through 55° guide vanes open for top two vanes.

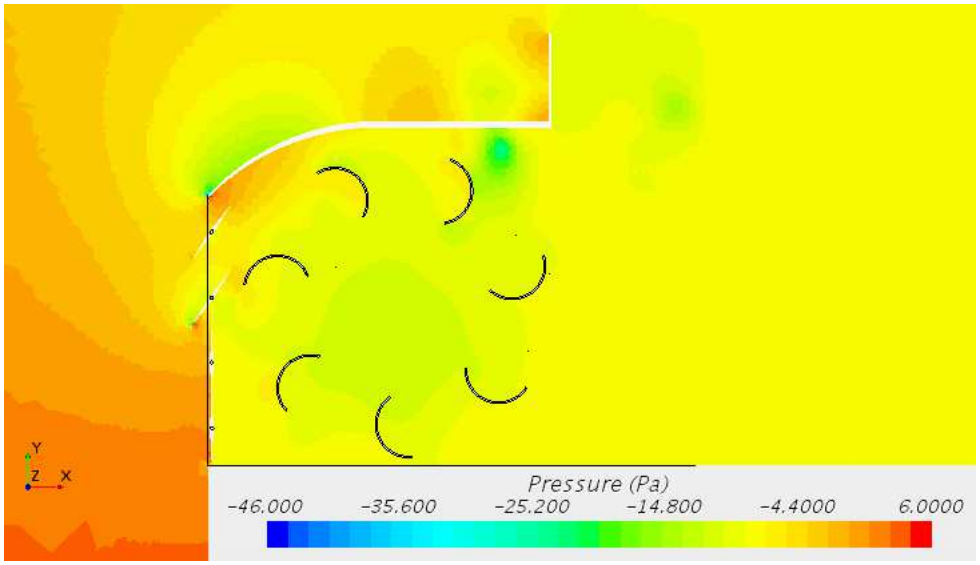

Figure 39: Mid-plane pressure colors of seven bladed turbine, through 55° guide vanes open for top two vanes.

The last study (case 2) had the bottom guide vane closed at an angle of $\emptyset = \mathbf{90}°$ and the rest of the vanes set at $\emptyset = \mathbf{55}°$. This second case not only presented a Cp value of 0.398 which was 19.5 % higher than the case with all the guide vanes open at $\mathbf{55}°$, but also had a Cp value similar to the original Cp value of 0.394 [37] which did not include guide vanes. This study proved to be very efficient as the open guide vanes directed the flow through the turbine at a higher velocity as shown in Figure 40.

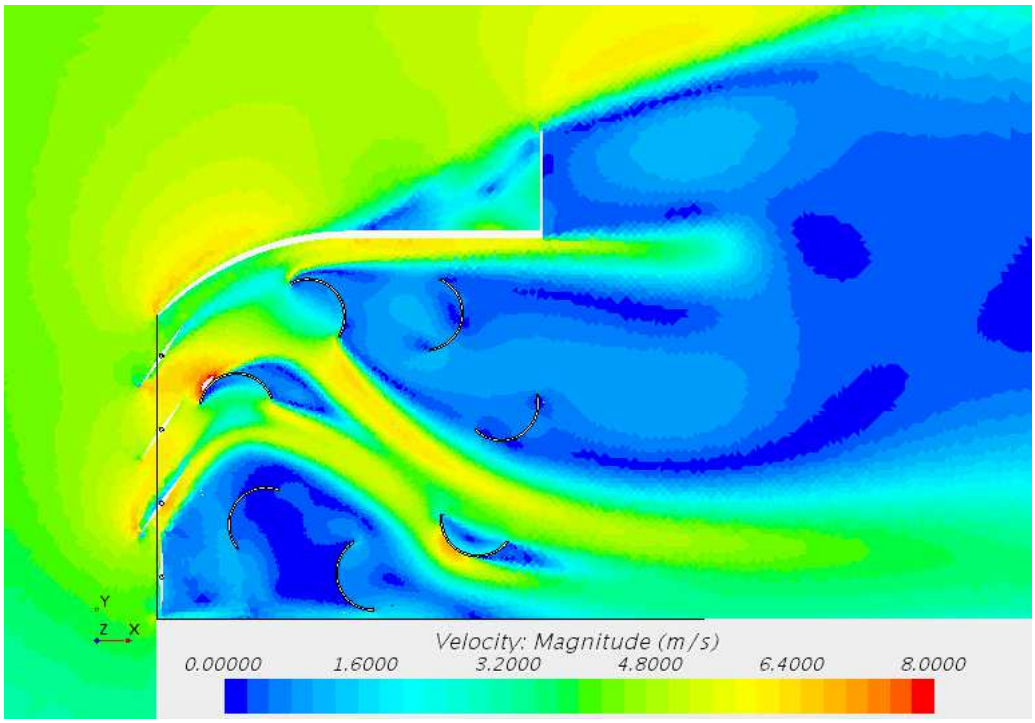

Figure 40: Mid-plane velocity colors of seven bladed turbine, through 55° guide vanes open for top three vanes.

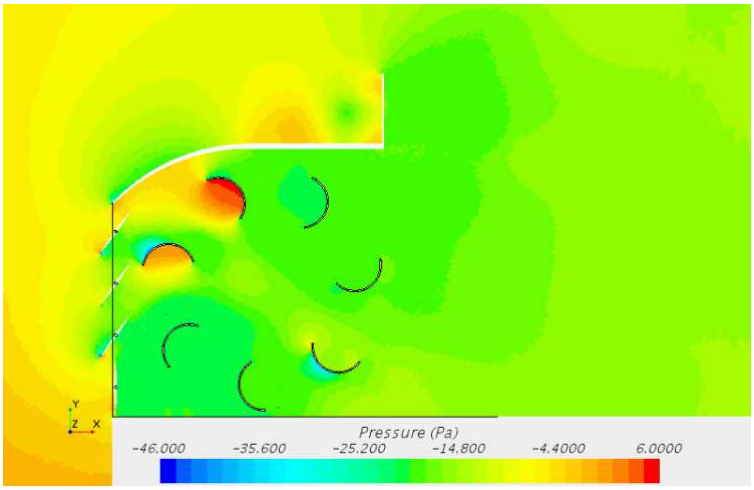

Figure 41: Mid-plane pressure colors of seven bladed turbine, through 55° guide vanes open for top two vanes.

The difference in the Cp values of the two cases may be due to the flow acceleration over the concave side of the blade in the upstream. For the first case, the inflow only affects part of the concave side of the blade as illustrated in Figure 42 (b). The second case positions the guide vanes to directly hit majority of the concave section of the blade as illustrated in Figure 42 (a). This helps start the turbine's rotation at a higher speed than the other cases. The pressure colors illustrated in Figure 41 also provide an indication where a high-pressure zone is developed on the inside part of the blade in the upstream.

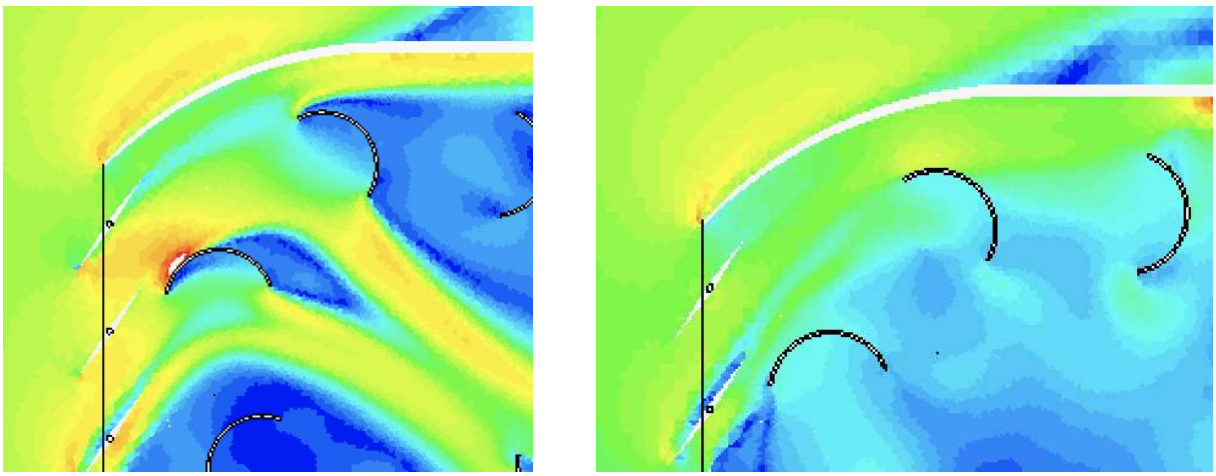

(a) (b)

Figure 42: Close up view of the midplane velocity colors on the upstream blade for (a) Bottom vane at $\emptyset = 90°$, and top three at $\emptyset = 55°$ (b) Bottom two guide vanes at $\emptyset = 90°$ and top two set at $\emptyset = 55°$.

Chapter 4: Conclusions

This thesis analyzes the flow over a novel configuration of a building-mounted seven bladed Savonius turbine enclosed inside a shroud with an integrated flange at the exit and four deflectable guide vanes attached at the entrance. After validating the methodology, 3D simulations of a building-mounted turbine with deflectable guide vanes are conducted. The power coefficient C_p is calculated based on CFD for guided vanes fixed at 35°, 45°, 55°, 65° and when certain guide vanes are set at 90° (closed) with respect to horizontal direction. The highest power coefficient value obtained for all guide vanes was 0.333 when all of the guide vanes are set at 55°, at the TSR of 0.5. It is slightly less than the C_p value 0.394 [37] at the same TSR obtained for the flow over a shrouded turbine without any guide vanes. Although the power coefficient tends to decrease by using guide vanes, these vanes provide the ability to control the flow through the turbine. It can be concluded that performance of the turbine decreases with the guide vanes at this TSR (0.5) but neighboring TSR values of 0.48 indicates a C_p value of 0.336.

However, setting the bottom vane to 90° while the top three are set at 55° proved to be the most efficient out of all cases. The C_p value of 0.398 succeeded in reaching the C_p value of 0.394 obtained without guide vanes. Having an equivalent C_p to the original design without deflectable guide vanes proves to be advantageous as these vanes can be closed for extreme wind speeds and can be partially closed for high winds allowing the turbine to function in these challenging conditions. These guide vanes can in fact increase the capacity factor of the turbine and therefore can increase the annual energy production.

4.1 Future Work

As a continuation of this study, future research can perform to compute the power coefficient of the turbine at different wind directions. Furthermore, the same Savonius turbine with the vanes attached can possibly be more effective for winds that are slewed to the turbine because they redirect the wind closer to the center of the turbine.

References

[1] E. Vine, "Breaking down the silos: the integration of energy efficiency, renewable energy, demand response and climate change," Energy Efficiency, pp. 49-63, 2008.

[2] W. Zhou, C. Lou, Z. Li, L. Lu and H. Yang, "Current status of research on optimum sizing of stand-alone hybrid solar-wind power generation systems," Applied Energy, pp. 380-389, 2010.

[3] A. Strupczewski, "Accident risks in nuclear-power plants," Applied Energy, pp. 79-86, 2003.

[4] M. Bazilian, T.Mai and S.Baldwin. Decision-making for High Renewable Electricity Future in the United States. Energy Strategy Review, 2(2014), ppg 326-328.

[5] A. Evans, V. Strezov and T. J. Evans, "Assessment of sustainability indicators for renewable energy technologies," Renewable and Sustainable Energy Reviews, pp. 1082-1088, 2009.

[6] Y. d. Boer, "The Energy Report 2013: 100% Renewable by 2050," 2013. [Online]. Available: http://wwf.panda.org/what_we_do/footprint/climate_carbon_energy/energy_solutions22/renewable_energy/sustainable_energy_report/.

[7] R. Bãnos, F. Manzano-Agugliaro, F. G. Montoya, C. Gil, A. Alcayde and J. Gómez, "Optimization methods applied to renewable and sustainable energy: A review," Renewable and Sustainable Energy Reviews, pp. 1753-1766, 2011.

[8] "Renewables 2010 Global Status Report," Paris, 2017.

[9] G. W. E. Council and G. International, "Global Wind Energy Outlook," 2010.

[10] Conserve Energy Future, "Disadvantages of Renewable Sources of Energy," [Online]. Available: http://www.conserve-energy-future.com.

[11] S. Eriksson, H. Bernhoff and M. Leijon, "Evaluation of different turbine concepts for wind power," Renewable and Sustainable Energy Reviews, vol. 12, no. 5, pp. 1419-1434, 2006F

[12] I. Paraschivoiu, Wind Turbine Design with Emphasis on Darrieus Concept, Montreal: Polytechnic International Press, Canada, 2002.

[13] M. C. Claessens, "The Design and Testing of Airfoils for Application in Small Vertical Axis Wind Turbines," Delft University of Technology, Amsterdam, 2006

[14] J. Cace, E. Horst, K. Syngellakis, M. Niel, P. Clement, R. Heppener, and E. Peirano. Urban wind turbines, Guidelines for small wind turbines in the built environment, 2016 (2007), p. 41

[15] E. Hau, Renewable Energy, Fundamental, Technology, Applications and Economics, Berlin Heidelberg: Springer-Verlag, 2006.

[16] M. Ragheb. Safety of wind systems. Technical report, 2012.

[17] S. Sicklinger, C. Lerch and R. Wuchner. Fully coupled co-simulation of a wind turbine emergency brake maneuver. Journal of Wind Engineering and Industrial Aerodynamics, 144 (2105), ppg 134-145

[18] I. Paraschivoiu (2002). Wind Turbine Design with Emphasis on Darrieus Concept, Presses Internationales Polytechnique, Canada.

[19] J.L. Acosta, K. Combe, S. Djolic and I. Hernando-Gil (2012). Performance assessment of micro and small-scale wind turbines in urban areas, IEEE Systems Journal, Volume: 6 Issue: 1, 152-163. doi:10.1109/JSYST.2011.2163025

[20] A.S. Bahaj, L. Myers andP. A James. (2007). Urban electricity generation: influence of micro-wind turbine output on electricity consumption in buildings, Energy and Buildings, Volume 39, Issue 2, 154- 165. doi: 10.1016/j.enbuild.2006.06.001

[21] N. Zadeh, M. Komeili and M. Paraschivoiu (2014). Mesh Convergence Study for 2D Straight–Blade Vertical Axis Wind Turbine Simulations and Estimation for 3D Simulations, Transactions of the Canadian Society for Mechanical Engineering, 38 (4), ppg: 487-504.

[22] L. Ledo, P.B. Kosasih and P. Cooper. (2010). Roof mounting site analysis for micro-wind turbines, Renewable Energy, Volume: 36, Issue: 5, 1379-1391. doi: 10.1016/j.renene.2010.10.030

[23] A. Dragorimescu (2011). Performance Assessment of a small wind Turbine with Crossflow Runner by Numerical Simulations", Renewable Energy, 36, 957-965, doi: 10.1016/j.renene.2010.07.028

[24] B. Sanderse, S. P. v. d. Pijl and B. Koren, "Review of computational fluid dynamics for wind turbine wake aerodynamics," Wind Energy, no. 14, pp. 799-819, 2011.

[25] C. Song, Y. Zheng, Z. Zhao, Y. Zhang, C. Li and H. Jiang, "Investigation of meshing strategies and turbulence modesl of computational fluid dynamics simulations of vertical axis wind turbines," Journal of Renewable and Sustainable Energy, no. 7, 2015.

[26] E. Sagol, M. Reggio and A. Ilinca, "Assessment of Two-Equation Turbulence Models and Validation of the Performance Characteristics of an Experiemental Wind Turbine by CFD," ISRN Mechanical Engineering, 2012.

[27] E. S. Holdredge and B. H. Reed, "Pressure Distribution on Buildings," Texas Engineering Experimental Station, College Station, 1957.

[28] B. H. Evans, "Natural Air Flow around Buildings," Texas Engineering Experimental Station, College Station, 1957.

[29] C. Song and J. He, "Computation of Wind Flow around a Tall Building and the Large-Scale Vortex Structure," Journal of Wind Engineering and Industrial Aerodynamics, no. 46; 47, pp. 219-228, 1993.

[30] A. Razak, A. Hagishima, N. Ikegaya and J. Tanimoto, "Analysis of airflow over buildng arrays for assessment of urban wind environment," Building and Environment, no. 59, pp. 56-65, 2013.

[31] I. Abohela, N. Hamza and S. Dudek (2013). "Effect of roof shape, wind direction, building height and urban configuration on the energy yield and positioning of roof mounted wind turbines", Renewable Energy, 50, 1106-1118. doi: 10.1016/j.renene.2012.08.068

[32] Y. Ohya, and T. Karasudani and X. Zhang (2010). A Shrouded Wind Turbine Generating High Output Power with Wind-Lens Technology", Energies, 3, 634-649. doi: 10.3390/en3040634

[33] A. Dilimulati, T. Stathopoulos and M. Paraschivoiu (2017), Wind Turbine Designs for Urban Applications: A Case Study of the Shrouded Diffuser Casing for Turbines, *submitted* Journal of Wind Engineering & Industrial Aerodynamics, 288-291. Available from: www.winercost.com/cost_files/WINERCOST17_Proceedings_Book.pdf

[34] T. Matsushima, S. Takagi and S. Muroyama. Characteristics of a highly efficient propeller type small wind turbine with a diffuser. Renewable Energy, 31 (2006), pp. 1343-1354. doi: 10.1016/j.renene.2005.07.008

[35] A. El-Zahaby, A.E. Kabeel, S.S Elsayed and M.F Obiaa. CFD analysis of flow fields for shrouded wind turbine's diffuser model with different flange angles. Alexandria Engineering Journal, 56 (2017), ppg 171-179. doi: 10.1016/j.aej.2016.08.036

[36] P. Larin, M. Paraschivoiu, and C. Aygun, C. (2016). CFD based synergistic analysis of wind turbines for roof mounted integration", J.Wind Eng.Ind.Aerodyn.,156, 1-13. doi: 10.1016/j.jwela.2016.06.007

[37] A. Krishnan and M. Paraschivoiu (2016). 3D analysis of building mounted VAWT with diffuser shaped shroud", Sustainable Cities and Society, 27, 160-166. doi: 10.1016/j.scs.2015.06.006

[38] M. Mohamed, G. Janiga, E. Pap, and D. Thevenin. Optimal blade shape of a modified Savonius turbine using an obstacle shielding the returning blade. Energy Conversion and Management 2011;52(1):236-242. doi: 10.1016/j.enconman.2010.06.070

[39] B. Wahyudi, S.Sudjito, and H. Hoeijmakers. Optimization design of Savonius diffuser blade with moving deflector for hydrokinetic cross flow turbine rotor. Energy Procedia 2015; 68:244-253. doi: 10.1016/j.egypro.2015.03.253

[40] T. Hayashi, L. Yan and H. Yutaka. Wind tunnel tests on a different phase three-stage Savonius rotor. JSME International Journal Series B 2005;48(1): 9-16. doi: 10.1299/jsmeb.48.9

[41] B. Patankar, R. Tyagi, D. Kiss, A.B. Suma, PowerNEST concept Evaluation of an integrated roof wind energy system for urban environments. J. Phys. Conf., 753 (2016), p. 102007

[42] A. Hemami 2011, Wind Turbine Technology, Cengage Learning, Clifton Park, New York

[43] Siemens, STAR-CCM+ User Guide, Version 12.02A, Siemens PLM Software, 2017.

[44] "The Drag Coefficient" [Online] Available: https://www.grc.nasa.gov/www/k-12/airplane/dragco.html

[45] "Saffir-Simpson Hurricane Wind Scale" [Online] Available: http://www.nhc.noaa.gov/aboutsshws.php

[46] C. Robert, Juvinall and M. Kurt, "Fundamentals of Machine Component Design", Wiley; 5th edition. Appendix D Pg. 851

[47] C. Robert, Juvinall and M. Kurtt "Fundamentals of Machine Component Design", Wiley; 5th edition. Pg. 274-276

[48] R. Smith and S. Killa. Bahrain World Trade Center (BWTC): the first large-scale integration of wind turbines in a building. Tall and Special Buildings 2007; 16(4): ppg 429-439. doi: 10.1002/tal.416

[49] Durbin and G. Medic, Fluid Dynamics with a Computational Perspective. Cambridge University Press, 2007.

[50] B. Belabes, A. Youcefi and Marius Paraschivoiu. Numerical investigation of Savonius wind turbine farms. Journal of Renewable and Sustainable Energy 2016;8(5) doi: 10.1063/1.4963688

[51] V. Samson 2017, 'Unsteady and Three-Dimensional CFD Simulation of a Darrieus Turbine on the Roof of a Building, Concordia University'. MASc, Concordia Univeristy, Montreal.

[52] R. Sheldahl, "Comparison of Field and Wind Tunnel Darrieus Wind Turbine Data," Sandia National Laboratory, 1981.